

REVIEW PAPER

CONTRIBUTIONS TO DEVELOPMENTS OF PHOTOELECTRON SPECTROSCOPY AND X-RAY ABSORPTION FINE STRUCTURE APPLIED TO MATERIALS STUDIES

NGUYEN VAN HUNG[†]

Department of Physics, VNU University of Science, 334 Nguyen Trai, Hanoi, Vietnam

E-mail: [†]hungnv@vnu.edu.vn

Received 11 January 2021

Accepted for publication 09 March 2021

Published 15 April 2021

Abstract. *This work reviews the contributions of author to the developments and applications of Photoelectron Spectroscopy (PES) and X-ray Absorption Fine Structure (XAFS) applied to materials studies. Focusing on Angle Resolved PES (ARPES) the energy distribution is discussed for angle-resolved photoemission from valence bands of single crystals. The important influence of the spectrometer angle of acceptance on the results of X-ray PES (XPS) is investigated in detail. The Plane Density of States (PDOS) is introduced as a new property of the electronic structure. Most meaningful contributions to XAFS consist of the developments of multiple-scattering and anharmonic XAFS theories. Anharmonic correlated Einstein model (ACEM) and anharmonic correlated Debye model (ACDM) have been derived to obtain Debye-Waller factors (DWF) presented in terms of cumulant expansion which describes the thermodynamic properties and anharmonic effects in XAFS of substances contributing to their accurate structural determination. The anharmonic effective potential (AEP) procedure and first shell near neighbor contributions approach have developed to include many-body effects in the one-dimensional model by a simple measure. Based on DWFs a thermodynamic lattice theory has been derived for studying melting curve and eutectic points of binary alloys. Several applications of the derived methods are performed and the good agreement of the calculated results with experiment illustrate the advantages and efficiencies of the achieved developments.*

Keywords: ARPES and PDOS, XAFS, DWF and cumulant expansion, ACEM and ACDM, AEP procedure, advanced method, temperature and pressure dependence, melting temperature.

Classification numbers: 79.60.-i; 78.70.Dm; 61.05.C-; 63.70.th.

I. INTRODUCTION

Both photoelectron spectroscopy (PES) and X-ray absorption fine structure (XAFS) have resulted based on photoelectrons emitted from an absorbing atom due to the interaction of light photons with materials. The PES appears if the photoelectron has sufficient energy to go out the material surface, while XAFS is the result of interference of the wave of the emitted photoelectron with the one coming back to the absorbing atom after scattering by the other surrounding atoms. The PES provides information on electronic structure, see for example [1–4], while XAFS gives information on the accurate thermodynamic properties, anharmonic effects, and structural determination of substances, see for example [5–10]. Thanks to many efforts being made for the investigations in these fields [1–80] both PES and XAFS have developed into the powerful procedures for material studies.

The purpose of this work is to review several contributions of the author to the developments of PES and XAFS applied to materials studies. They are presented in Section II. Focusing on angle-resolved PES (ARPES) the energy distribution is discussed for APES from valence bands of single crystals. The important influence of the spectrometer angle of acceptance on the results of X-ray PES (XPS) is investigated in detail. The Plane Density of States (PDOS) is introduced as a new property of the electronic structure. The most meaningful contributions to XAFS spectroscopy consist of the developments of multiple-scattering and anharmonic XAFS theories. Anharmonic correlated Einstein model (ACEM) and anharmonic correlated Debye model (ACDM) have been derived to obtain Debye-Waller factors (DWF) presented in terms of cumulant expansion whose cumulants describe thermodynamic properties and anharmonic effects in XAFS of substances contributing to their accurate structural determination. Here, the anharmonic effective potential (AEP) procedure and the first shell near neighbor contributions approach (FSNNCA) have developed to include the many-body effects in the present one-dimensional model by a simple measure. The ACEM has further developed for different cases such as the classical ACEM, the pressure-dependent ACEM, the ACEM for doping materials compared to Mössbauer studies, the ACEMs for isotopic, pressure and impurity effects. A method has developed for studying correlation effects. Statistical moment method (SMM) has also been involved to study temperature-dependent DWFs of semiconductors and compounds. Based on ACEM an advanced method has been derived for the theoretical and experimental XAFS studies of thermodynamic properties, anharmonic effects and structural determination of materials that simplifies and reduces XAFS calculations and measurements based on second cumulant. From DWFs the thermodynamic lattice theory has been derived for studying melting curve and eutectic points of binary alloys. Many applications of the derived methods have been performed and the good agreement of the theoretical results with experiments illustrates the advantages and efficiencies of the achieved developments. The conclusions are presented in Sec. III.

II. CONTRIBUTIONS

II.1. Development of angle-resolved photoelectron spectroscopy [11–13]

II.1.1. *Intensity of ARPS in three-step model*

In order to derive the intensity of ARPS in three-step model it is important to specify probability of propagating electron from the initial state $|i\rangle = |k\nu_i\rangle$ having energy E_i to final state

$|f\rangle = |kv_f\rangle$ having energy E_f scattered to $|f'\rangle$ and then emitted through the surface to have the momentum $\mathbf{P}_a = \sqrt{2mE}\mathbf{e}_s$ with \mathbf{e}_s being the orientation of spectrometer under the action of one photon with frequency ω as

$$\gamma_{i \rightarrow \mathbf{P}_a} = \sum_{f, f'} \gamma_{i \rightarrow f} P_{ff'}^{scatt.} P_{f' \mathbf{P}_a}^{surf.}, \quad \gamma_{i \rightarrow f} = \frac{2\pi}{\hbar} |\langle \tilde{f} | W | i \rangle|^2 \delta(E_f - E_i - \hbar\omega). \quad (1)$$

Consequently, the intensity of photoelectron spectrum of ARPES in the present derived theory has resulted as a new contribution

$$\begin{aligned} \tilde{I}(\omega, \mathbf{e}, \mathbf{q}; \mathbf{b}_i, n, \Phi'; E, \mathbf{e}_s) dE d\Omega_P &= I(\omega, \mathbf{e}, \mathbf{q}; \mathbf{k}, \mathbf{g}_P, E) dE d\Omega_P \\ &= \frac{\Omega m \sqrt{2mE}}{(2\pi)^2 \hbar^4} \int^{resol.} d^3 \mathbf{P} \sum_{v_i, v_f} \left| \langle \mathbf{k} v_i | W | \mathbf{k} v_f \rangle \right|^2 \langle \mathbf{k} v_f | \mathbf{k} + \mathbf{g}_P \rangle^2 \delta(E - E(\mathbf{k}, v_i) - \hbar\omega) \delta_{E_f, E}. \end{aligned} \quad (2)$$

which depends on the properties of photon (ω , \mathbf{e} , \mathbf{q}), parameters of crystal (\mathbf{b}_i , n , Φ') and orientation of spectrometer (E , \mathbf{e}_s). Here, \mathbf{q} is wave vector, \mathbf{e} is polarization vector, $\mathbf{P} = \mathbf{k}(\mathbf{P}, \mathbf{b}_i) + \mathbf{g}_P(\mathbf{P}, \mathbf{b}_i)$, \mathbf{g}_P is reciprocal lattice vector, Φ' is potential wall, Ω is normalization volume. The summation over the final states is expressed by integration over the momentum- and \mathbf{k} -intervals whose values are specified by dE and $d\Omega_P$ which are indexed by the resolution of spectrometer.

II.1.2. Plane density of states as a new value of ARPES

The analysis of photoelectron intensity given by Eq. (2) for ARPES can be performed based on the experimental conditions. In the angle of acceptance $\Delta\theta$ and energy resolution ΔE all electrons contribute to photoelectron spectrum. They have momentums with the value (ΔP) and the direction (ΔP_\perp) lying in a certain interval around \mathbf{P}_a . These values are valued for the normally used experimental values of $\Delta\theta$ and ΔE .

Considering the size of Brillouin zone (BZ) the following conclusions have been resolved: - For UPS, the momentum interval is small compared to the size of BZ so that it is in a good approximation the contribution of one point from BZ is measured, and - For XPS, the length of momentum vector is exactly fixed but the value of ΔP_\perp is of the size of BZ, then the contributions of electronic states with \mathbf{k} -vectors on a surface are measured which is approximated to a plane because the value of \mathbf{P}_a is great compared to the size of BZ. This leads to further consideration of a cross-plane in the first BZ. Based on the above considerations we calculate

$$\int^{resol.} d^3 \mathbf{P} = dP_\perp \int^{resol.} d^2 \mathbf{P} = \frac{m\hbar^2}{p} dE \int^{resol.} d^2 k \approx \frac{m\hbar^2}{p} dE \int_{BZ} d^3 k \delta(\mathbf{e}_s \cdot \mathbf{k} - k_0). \quad (3)$$

In XPS, there is very small difference between vectors \mathbf{e}_s , $\mathbf{P}/|\mathbf{P}|$ and $\mathbf{g}_P/|\mathbf{g}_P|$, as well as it is possible to describe $k_0 = P - g_P$. Then, the intensity (2) for ARPES is simplified as

$$I(\omega, \mathbf{e}, \mathbf{q}; \mathbf{k}, \mathbf{g}_P, E) dE d\Omega_P = \frac{E^2 (\mathbf{e} \cdot \mathbf{P})^2}{2\pi\hbar\omega} \sum_{v_i} \int_{BZ} d^3 k |\phi_i(P)|^2 \delta(E - E(k, v_i) - \hbar\omega) \delta(\mathbf{e}_s \cdot \mathbf{k} - k_0), \quad (4)$$

which for constant matrix element contains the plane density of state (PDOS) as a new electronic property for ARPES

$$n_P(\varepsilon, k_0, \mathbf{e}_s) = \sum_{v_i} \int_{BZ} d^3 k \delta(E - E(k, v_i) - \hbar\omega) \delta(\mathbf{e}_s \cdot \mathbf{k} - k_0). \quad (5)$$

This PDOS depends on the orientation of spectrometer described by vector \mathbf{e}_S showing the ARPES. It characterizes the number of electronic states of energy interval dE lying in the plane. By integration over k_0 it leads to the usual density of states (DOS)

$$n(\varepsilon) = \int_{BZ} d^3k_0 n_P(\varepsilon, k_0, \mathbf{e}_S). \quad (6)$$

II.1.3. Numerical results and discussions

The calculation of PDOS is performed for Be having hexagonal structure whose BZ is presented in Fig. 1. This calculation has been performed for planes of $1/24$ of BZ (Γ AHLMK) (Fig. 1a) using band structure.

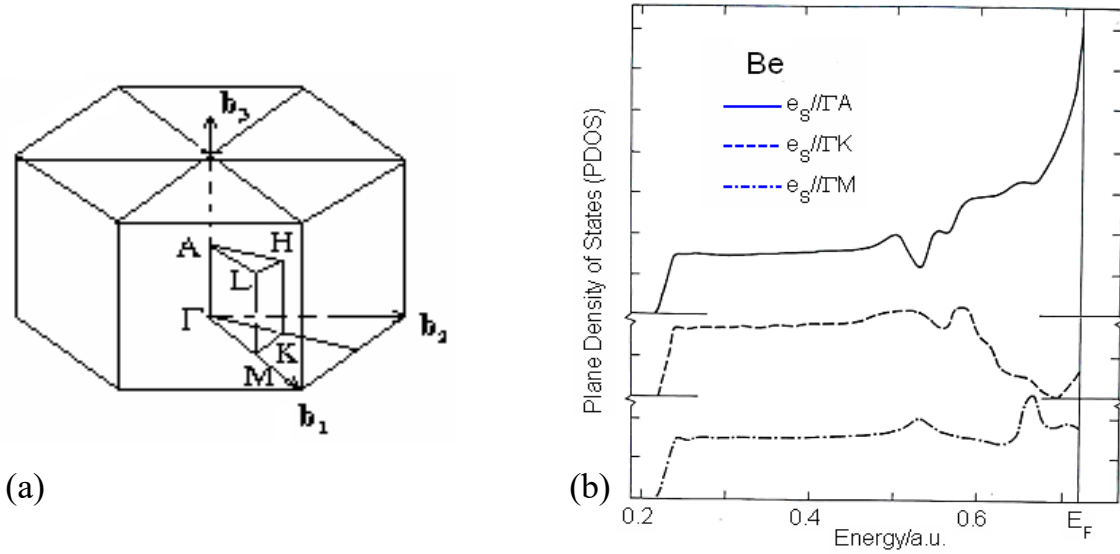


Fig. 1. (a) BZ of Be with its $1/24$ (Γ AHLMK) for calculation of PDOS and (b) comparison of PDOS of three directions: $\mathbf{e}_S//\Gamma A$, $\mathbf{e}_S//\Gamma K$, and $\mathbf{e}_S//\Gamma M$.

The calculated PDOS of three directions: (1) $\mathbf{e}_S//\Gamma A$, (2) $\mathbf{e}_S//\Gamma K$, and (3) $\mathbf{e}_S//\Gamma M$ are presented in Fig. 1.b. Their differences describe the ARPES characterizing the differences of electronic structures in different planes perpendicular to different planes in the first BZ of the considered crystal. It is different from usual DOS which are the same for all directions.

II.2. Development of XAFS theory in single and multiple scattering [14–17]

II.2.1. Quantum theory on scattering in XAFS, partial wave procedure

The main effect in XAFS process is scattering of photoelectron by the atoms surrounding the absorber and scattering atoms so that it is important to determine the wave function of photoelectron in this process. In quantum theory this function is the solution of Schrödinger equation for one electron in the potential $V(r)$

$$\left[-\frac{\partial^2}{\partial r^2} + W(r) \right] \Psi = k^2 \Psi; \quad V(r) = \frac{\hbar}{2m} W(r), \quad E = \frac{\hbar k^2}{2m}, \quad (7)$$

which can be transmitted into Lippman-Schwinger equation of integral form

$$\Psi(\mathbf{r}) = \phi(\mathbf{r}) + \int d\mathbf{r}' G_0(\mathbf{r}, \mathbf{r}') W(\mathbf{r}') \Psi(\mathbf{r}'). \quad (8)$$

It is the fundamental equation of scattering problem including beside plane wave $\phi(\mathbf{r})$ the second part describing scattering the outgoing wave describing spherical wave after scattering by the potential $V(\mathbf{r}')$. Here Green function of free electron has the form

$$G_0(\mathbf{r}, \mathbf{r}') = \frac{\exp(ik|\mathbf{r} - \mathbf{r}'|)}{4\pi|\mathbf{r} - \mathbf{r}'|}. \quad (9)$$

If potential $V(\mathbf{r})$ is spherical symmetric the wave function is the superposition of partial functions in the form

$$\Psi(\mathbf{r}) = \sum_L e^{i\delta_l} \Phi_l Y_L(\mathbf{r}). \quad (10)$$

where outside the muffin-tin Φ_l is the linear superposition of spherical Bessel function J_l and Bessel Neuman function n_l . They are normalized based on the conditions

$$\Phi_l(r) = \begin{cases} j_l(kr), & \text{for } V(r) = 0 \\ \cos \delta_l j_l(kr) - \sin \delta_l n_l(kr), & \text{for } V(r) \neq 0 \end{cases} \quad (11)$$

Here Φ_l satisfies asymptotic condition

$$\Phi_l(r \rightarrow \infty) = \frac{1}{kr} \sin\left(kr - l\frac{\pi}{2} + \delta_l\right). \quad (12)$$

Using spherical Hankel function I in the form

$$h_l(kr) = j_l(kr) + n_l(kr), \quad (13)$$

we obtain

$$\Phi_l(kr) = j_l(kr) e^{i\delta_l} + i \sin \delta_l h_l(kr). \quad (14)$$

Substituting Eq. (14) into Eq. (10) the wave function outside the muffin-tin in this scattering process has resulted as

$$\Psi(\mathbf{r}) = \sum_L C_L [j_l(kr) + T_l h_l(kr)] Y_L(\mathbf{r}); \quad r > r_{MT}, \quad (15)$$

$$T_l = -ikt_l = i \sin \delta_l e^{i\delta_l} = ik \int dr r^2 j_l(kr) W(r) \Phi_l(r), \quad (16)$$

where T_l is the scattering matrix and δ_l is scattering phase.

According to Eq. (15) the scattering is happened in the following process: Each coming wave described by the first component $\phi = j_l Y_L$ creates a scattering wave described by the second component $\Psi_S = T_l h_l Y_L$. This is the clear scattering process caused by a potential.

If suppose that absorber lies in the origin of coordinate system and emitted photoelectron has spherical wave and scattering potential is located at \mathbf{R} . Then the spherical wave coming in scattering potential has the form

$$\Psi(\mathbf{r}) = \phi_\lambda(\mathbf{r}) = h_\lambda(k|\mathbf{r} + \mathbf{R}|) Y_\lambda(\mathbf{r} + \mathbf{R}). \quad (17)$$

Therefore, both wave of photoelectron and scattering wave have the form given by Eq. (17) or it superposition.

II.2.2. Development of some approximations on scattering theory in XAFS

a. Small Scattering Center Approximation (SSCA)

In this SSCA we suppose that R_{MT} is much smaller than the distance R between atoms. Then the wave function given by Eq. (17) will be approximated to the plane wave

$$h_l(x) \approx \frac{e^{ix}}{i^{l+1}x}, \quad x \gg 1, \quad \phi_\lambda(\mathbf{r}) = h_\lambda(k|\mathbf{r} + \mathbf{R}|) Y_\lambda(\mathbf{r} + \mathbf{R}) \approx h_\lambda(kR) Y_\lambda(\mathbf{R}) e^{i\mathbf{k}\mathbf{r}}, \quad (18)$$

where \mathbf{k}_R is wave vector penetrating in \mathbf{R} direction. Hence, the wave function in SSCA is the solution of the following Lippman-Schwinger equation

$$\Phi_k^0(\mathbf{r}) = e^{i\mathbf{k}\mathbf{r}} + \int d\mathbf{r}' G_0(\mathbf{r}, \mathbf{r}') W(\mathbf{r}') \Phi_k^0(\mathbf{r}'), \quad (19)$$

which satisfies the condition:

$$\Phi_k^0(\mathbf{r}) \rightarrow e^{i\mathbf{k}\mathbf{r}} + \frac{1}{r} f(\theta) e^{ikr} \quad (20)$$

having scattering amplitude $f(\theta)$ depending on scattering angle $\theta = (\mathbf{r}, \mathbf{k})$.

Based on the equivalence between Eqs. (19) and (20) the scattering wave function in SSCA has resulted as

$$\Psi_S(\mathbf{R}) = \frac{1}{r} h_\lambda(kR) Y_\lambda(\mathbf{R}) f(\theta) e^{i\mathbf{k}\mathbf{r}}, \quad f(\theta) = \frac{1}{ik} \sum_l (2l+1) T_l P_l(\cos \theta), \quad (21)$$

where P_l is polinom Legendre.

Hence, scattering phases contribute only to the scattering amplitude $f(\theta)$ and all components depending on momentum are contained in this $f(\theta)$. Therefore, there is no requirement on increasing of the scattering phase number when energy increases as in the partial wave procedure.

b. Modified SSCA (MSSCA)

The limitation of the SSCA is neglecting of spherical form of wave face so that it can be well applied only to the case for energy $E \geq 400\text{eV}$. To solve this problem the MSSCA (Modified SSCA) has developed. In this approximation the Green function in momentum expansion has the form

$$G_0(\mathbf{r}, -\mathbf{R}) = -i\hbar \sum_L j_l(kr) h_l(kR) Y_L^*(\mathbf{r}) Y_L(-\mathbf{R}), \quad R > r, \quad (22)$$

related with Hankel function as

$$h_0(k|\mathbf{r} + \mathbf{R}|) = -\frac{4\pi}{ik} G_0(\mathbf{r}, -\mathbf{R}) = 4\pi \sum_L j_l(kr) h_l(kR) Y_L^*(\mathbf{r}) Y_L(-\mathbf{R}). \quad (23)$$

As in the approximation described by Eq. (17) we obtain

$$\phi_\lambda(\mathbf{r}) = h_\lambda(k|\mathbf{r} + \mathbf{R}|) Y_\lambda(\mathbf{r} + \mathbf{R}) \approx h_\lambda(kR) Y_\lambda(\mathbf{R}) \frac{h_0(k|\mathbf{r} + \mathbf{R}|)}{h_0(kR)}. \quad (24)$$

Using further Eqs. (23) and (24) we obtain the incident in the following presentation

$$\phi_\lambda = \frac{h_\lambda(kR) Y_\lambda(\mathbf{R})}{h_0(kR)} 4\pi \sum_L j_l(kr) h_l(kR) Y_L^*(\mathbf{r}) Y_L(-\mathbf{R}). \quad (25)$$

Calculation as for Eq. (11) and using the relations

$$Y_L(-\mathbf{R}) = (-i)^l Y_L(\mathbf{R}), 4\pi \sum_m Y_L^*(\mathbf{r}) Y_L(-\mathbf{R}) = (2l+1) P_l(\cos \theta), j_l(kr) = ie^{i\delta_l} \sin \delta_l h_l(kr), \quad (26)$$

the scattering wave function in MSSCA has resulted as

$$\Psi_S = \frac{1}{r} h_\lambda(kR) Y_\lambda(\mathbf{R}) f_{eff}(r, R, \cos \theta) e^{ikr}, \quad (27)$$

$$f_{eff}(r, R, \cos \theta) = \frac{1}{ik} \sum_l (2l+1) T_l P_l(\cos \theta) \frac{(-1)^l h_l(kR) h_l(kr)}{h_0(kR) h_0(kr)}. \quad (28)$$

Hence, in MSSCA the effective scattering amplitude given by Eq. (28) has been introduced as a new development in XAFS theory. While scattering amplitude f depends only on scattering angle θ , the f_{eff} in MSSCA depends not only on θ but also on the distances R to emitter and r to observer. For great distances R and r to scattering center according to the approximation f_{eff} is transmitted to the normal scattering amplitude $f(\theta)$.

II.2.3. Curved-wave and multiple-scattering XAFS theory

XAFS is the effect of the final scattering state. Here, photoelectron penetrates in a surrounding atomic cluster so that it is scattered by these atoms before coming to interference with the wave emitted from absorbing atom. The result of this interference creates XAFS spectrum. Therefore, we will derive a XAFS theory including all scattering processes presented in the above sections. For this purpose, we describe the X-ray absorption coefficient in the form

$$\gamma = \frac{2\pi}{\hbar} \langle \Phi_c Y_{L_c} | \mathbf{e} \cdot \mathbf{r} (-1/\pi) \text{Im} G(\mathbf{r}, \mathbf{r}') \mathbf{r}' \cdot \mathbf{e} | \Phi_c Y_{L_c} \rangle, \quad (29)$$

Here, \mathbf{e} is polarization vector, initial state is core state (c), final state is described by Green function of total system containing scattering matrix $t^{\mathbf{R}}$ caused by the atom located at \mathbf{R} . If absorber atom is located at the coordinate origin ($\mathbf{R}_0 = 0$) the Green function of total system has the form

$$G(\mathbf{r}, \mathbf{r}') = G_a(\mathbf{r}, \mathbf{r}') + \sum_{R_1 \neq 0} G_a t^{R_1} G_a + \sum_{0 \neq R_2 \neq R_1 \neq 0} G_a t^{R_2} G_0 t^{R_1} G_a + \sum_{0 \neq R_3 \neq R_2 \neq R_1 \neq 0} G_a t^{R_3} G_0 t^{R_2} G_0 t^{R_1} G_a + \dots, \quad (30)$$

where the second term in the right describes the single-scattering and the others describe multiple-scatterings.

For spherical symmetry potential $V(r)$ the atomic Green function has the form

$$G_a(\mathbf{r}, \mathbf{r}') = -ik \sum_L \Phi_L(r) Y_L^*(\mathbf{r}) X_L(r) Y_L(\mathbf{r}'), \text{Im} G_a(\mathbf{r}, \mathbf{r}') = -k \sum_L \Phi_L(r) Y_L^*(\mathbf{r}) X_L(r) Y_L(\mathbf{r}'), \quad (31)$$

where Φ_L is regular and X_L is irregular solution of Schrödinger equation which satisfy all boundary conditions for $r > r_{MT}$.

After complicated calculations all terms given by Eq. (30) the Green function of total system resulted as

$$G(\mathbf{r}, \mathbf{r}') = G_a(\mathbf{r}, \mathbf{r}') + k \sum_{n=1}^N \sum_{CL} \sum_{L, L'} \Phi_l(r) Y_L(\mathbf{r}) e^{i(\delta_l + l\pi/2)} X_{LL'}^{CL} e^{i(\delta_{l'} - l'\pi/2)} \Phi_{l'}^*(r') Y_{L'}^*(\mathbf{r}'), \quad (32)$$

$$X_{LL'}^{CL} = -i^{l'-l+1} \prod_{i=1}^{\nu} \sum_{L_i} \left[G_{L_{i+1}L_i}(\mathbf{R}_{i+1} - \mathbf{R}_i) T_{L_i}^{R_i} \right] G_{L_1L'}(\mathbf{R}_1), \quad L_{\nu+1} = L, \quad \mathbf{R}_{\nu+1} = \mathbf{R}_0. \quad (33)$$

The condition given by Eq. (33) guarantees that the scattering loop is closed. The scattering process is characterized by the second term of Eq. (2.26) where N is the highest scattering order. The sum ν is over all from single to the n^{th} scattering orders for all closed loops (CL) in the sum over "CL". In each scattering way the scattering process is described as follows: Photoelectron emitted from absorber atom has phase shift $\delta_{l'}$ at state l' described by the spherical wave $\Phi_{l'}(r') Y_{L'}(\mathbf{r}')$. The scattering of this electronic wave by the other atoms is performed by $X_{LL'}^{CL}$ given by the first equation of Eq. (33) where the scattering by each atom is described by matrix T with the weight factor G characterizing the incident and scattering waves. Finally, electronic wave scattered by atom at \mathbf{R}_n to come back to the absorber atom is described by spherical wave $\Phi_l(r) Y_L(\mathbf{r})$ having the phase shift δ_l in the state l .

Substituting Green function (32) into (29) the absorption coefficient has resulted as

$$\gamma = \frac{2k}{\hbar} \left\{ \sum_l |\langle \Phi_c | r | \Phi_l \rangle|^2 \sum_{mm_c} |\langle Y_{L_c} | \mathbf{e} \cdot \hat{\mathbf{r}} | Y_L \rangle|^2 - \text{Im} \left[\sum_{l'l'} \langle \Phi_c | r | \Phi_l \rangle \langle \Phi_{l'} | r' | \Phi_c \rangle \right. \right. \\ \left. \left. \times \sum_{n=1}^N \sum_{CL} \sum_{m_c, mm'} \langle Y_{L_c} | \mathbf{e} \cdot \hat{\mathbf{r}} | Y_L \rangle \langle Y_{L'} | \hat{\mathbf{r}} \cdot \mathbf{e} | Y_L \rangle X_{LL'}^{CL} e^{i(\delta_l + \delta_{l'} + l\pi/2 + l'\pi/2)} \right] \right\}, \quad \mathbf{r} = \mathbf{r}' / |\mathbf{r}|. \quad (34)$$

II.2.4. Multiple-scattering XAFS theory in approximations

XAFS spectra based on angular momentum expansion presented in the above section is exact. Unfortunately, the calculations will be very great, that is why we use the above derived MSSCA and SSCA to simplify the calculations of multiple-scattering XAFS spectra. The calculations of Green function of total system are similar to those in angular momentum expansion presented in subsection II.3.3 but with using the incident and scattering waves from these approximations.

The function Y_L in $h_l Y_L$ shows the penetrating direction of spherical wave so that it changes when photoelectron is scattered. If the penetrating direction is z-axis the necessary rotation to bring it into the scattering direction is performed based on the following expression

$$Y_{lm}^S(\mathbf{e}) = \sum_{m'} Y_{lm'}^{S'}(\mathbf{e}) D_{m'm}^l(\theta, \beta, \alpha), \quad D_{m'm}^l(\theta, \beta, \alpha) = e^{im'\theta} d_{m'm}^l(\beta) e^{im\alpha}, \quad (35)$$

where θ, β, α are Euler's angles. The notation $D_{m'm}^l(\mathbf{e}', \mathbf{e})$ is used for a rotation of coordinate system with the z-axis \mathbf{e} into the system with the axis \mathbf{e}' . After rotation the full wave is approximated by four spherical waves with the angular momentum $L = (0,0), (1,0), (1,\pm 1)$ which are used for the Reduced Angular Momentum Expansion (RAME) derived in this work.

The final expression for Green function in all three approximations, SSCA, MSSCA, RAME in the present derived multiple-scattering theory ($x_n = kR_n$) can be written as

$$G(\mathbf{r}, \mathbf{r}', E) = G_a(\mathbf{r}, \mathbf{r}', E) - k \sum_{CL} \sum_{LL'} \Phi_l(r) Y_L(\mathbf{r}) \sqrt{2l+1} D_{mm_n}^l(e_z, -\mathbf{R}_n) e^{i(\delta_l + l\pi/2)} \frac{e^{ix_n}}{x_n} \times S_{lL_n}(x_n) F_{L_n L_0 Z_{l'} L_0}(x_1) \frac{e^{ix_1}}{x_1} e^{i(\delta_{l'} + l'\pi/2)} \sqrt{2l'+1} D_{m_0 m'}^{l'}(\mathbf{R}_1, \mathbf{e}_z) Y_{l'}^*(r') \Phi_{l'}(r'), \quad (36)$$

where $F_{L_n L_0}$ describing the n^{th} order generalized scattering amplitude has the form

$$F_{L_n L_0} = f_{L_n L_{n-1}}(-x_n, x_{n-1}) \frac{e^{i|x_n - x_{n-1}|}}{|x_n - x_{n-1}|} f_{L_{n-1} L_{n-2}}(x_n - x_{n-1}, x_{n-1} - x_{n-2}) \cdots f_{L_1 L_0}(x_2 - x_1, x_1), \quad (37)$$

$$f_{L_2 L_1}(x_2, x_1) = \sum_l (2l+1) \sin \delta_l e^{i\delta_l} Z_{lL_2}(x_2) D_{m_1 m_2}^l(x_2, x_1) S_{lL_1}(x_1) \quad (38)$$

Substituting (36) into (29) the absorption coefficient γ in SSCA, MSSCA and RAME has resulted and the XAFS function is obtained from expression $\chi = (\gamma - \gamma_0) / \gamma_0$ which for K-edge has the form

$$\chi(k) = -\text{Im} \sum_{CL} W_{m_0, -m_n} e^{2i\delta_p} \frac{e^{ix_n}}{x_n} S_{lL_n}(x_n) (-1)^{m_n} F_{L_n L_0 Z_{1L_0}}(x_1) \frac{e^{ix_1}}{x_1}, \quad (39)$$

$$W_{mm'} = 9 \left\langle Y_{1m}^{R_1} \mid \mathbf{e} \cdot \hat{\mathbf{r}} \mid Y_{00} \right\rangle \left\langle Y_{00}^1 \mid \mathbf{e} \cdot \mathbf{r} \mid Y_{1m}^{R_1} \right\rangle, \quad (40)$$

and the values of S and Z in the above expressions are different for SSCA, MSSCA and RAME.

II.2.5. Numerical results and discussions

Numerical calculations have been carried out using the present theory and presented in Figs. 2 for (a) Total XAFS spectra of Ni calculated using MSSCA, SSCA, and (b) Fourier transform (FT) magnitude, imaginary FT of total XAFS spectra calculated using MSSCA, SSCA and of multiple scattering calculated using MSSCA for GaAs.

II.3. Development of theory on anharmonic contributions to XAFS [18–21]

II.3.1. Development of theory

The anharmonic effects have been discovered elsewhere [6] in experimental results for XAFS at high-temperatures influencing on the values obtained from XAFS. So, it is important and necessary to calculate and analyze these effects.

For including the anharmonic contributions, the expression of XAFS spectra can be obtained from the cumulant expansion approach [5] as

$$\chi(k) = \frac{NS_0^2}{kR^2} F(k) \exp \left[-2 \left\{ \frac{R}{\lambda(k)} + k^2 (\sigma_H^2 + \sigma_A^2) \right\} \right] \sin [2kR + \delta(k) + \Phi_A(k)], \quad (41)$$

where k and λ are the wave number and mean free path of emitted photoelectron, respectively, $F(k)$ is the real atomic backscattering amplitude, $\delta(k)$ is net phase shift, $\Phi_A(k)$ is anharmonic contribution to XAFS phase, N is atomic number of a shell, S_0^2 is the intrinsic loss factor due to many-electron effects, $R = \langle r \rangle$ with r being the instantaneous bond length between absorber and back-scatterer atoms.

At low temperatures, the mean square relative displacement (MSRD) $\sigma^2(T)$ describing disorders of atom position contains only the harmonic contribution σ_H^2 . As the temperature increases

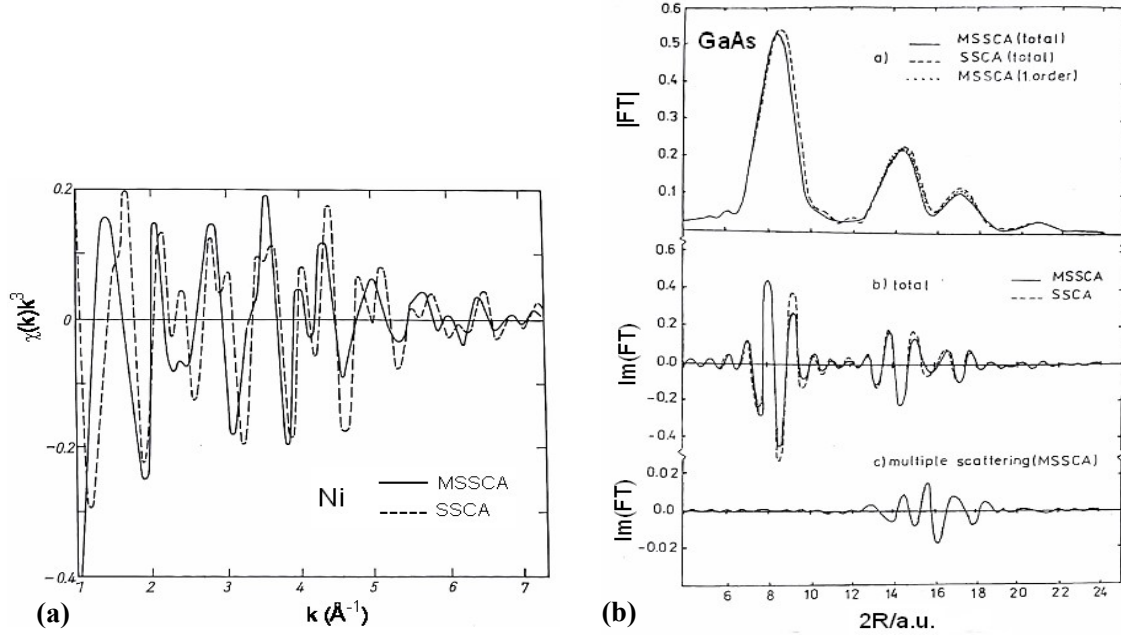


Fig. 2. (a) Total XAFS spectra including multiple scattering of Ni calculated using MSSCA, SSCA and (b) Fourier transform (FT) magnitude, imaginary FT of total XAFS spectra calculated using MSSCA, SSCA and of multiple scattering calculated using MSSCA for GaAs.

to a value above T_0 the vibration of atoms becomes anharmonic. This requires to add the anharmonic contributions $\sigma_A^2(k)$ to the MSD and $\Phi_A(k)$ to the phase of XAFS given by Eq. (41). By using the procedure presented in Ref. 18 they are given by

$$\sigma_A^2(R, T) = \beta(R, T) \sigma_H^2(R, T), \quad (42)$$

$$\Phi_A(k, T) = 2k \left[\Delta R(T) - 2\Delta\sigma^2(T) \left(\frac{1}{R} - \frac{1}{\lambda} \right) \right] - \frac{3}{4} \sigma^{(3)}(T) k^3, \quad (43)$$

$$\Delta\sigma^2(T) = \sigma_H^2(T) + \sigma_A^2(T) - \sigma_H^2(T_0), \quad \Delta R(T) = \frac{3k_B\Delta T}{8D\alpha}, \quad \Delta T = T - T_0, \quad (44)$$

$$\beta(R, T) = \frac{18\gamma_G M(T)}{(8D\alpha)^3} \left[(8D\alpha)^2 \left(\frac{k_B\Delta T}{R} \right) + 3(8D\alpha) \left(\frac{k_B\Delta T}{R} \right)^2 + 3 \left(\frac{k_B\Delta T}{R} \right)^3 \right], \quad (45)$$

$$M(T) = [\sigma_H^2(T) - \sigma_H^2(T_0)] / \sigma_H^2(T), \quad (46)$$

where $\sigma^{(3)}$ is the third cumulant [5], ΔR is linear thermal expansion, γ_G is Grüneisen parameter, k_B is Boltzmann constant, D and α are Morse potential parameters [57].

II.3.2. Numerical results and discussions

The derived expressions are now used for numerical calculations for Cu using its Morse potential parameters [57]. Figs. 3 illustrate (a) the dependence of anharmonic factor $\beta(R, T)$ on the temperature T and distance R between the absorbing atom and its neighbors located in spherical

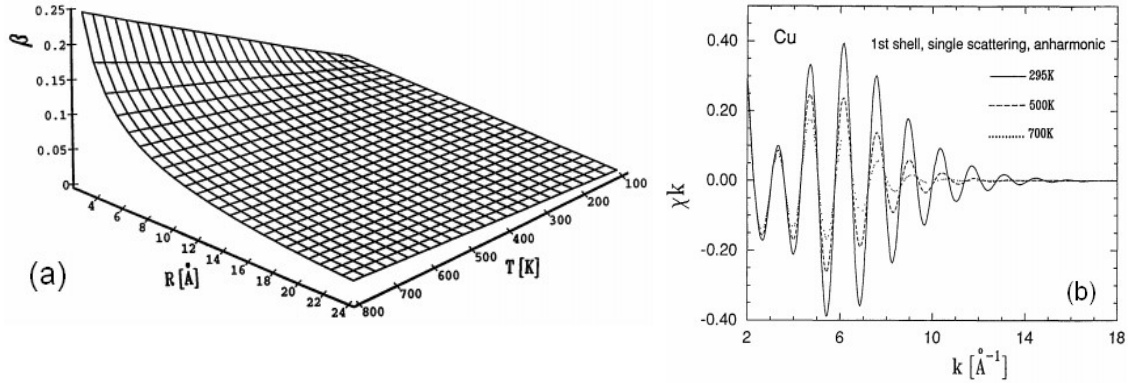


Fig. 3. (a) Dependence of anharmonic factor $\beta(R,T)$ on distance R and temperature T and (b) XAFS spectra $\chi(k,T)$ at 295 K, 500 K and 700 K calculated using the present theory.

shells and (b) temperature dependence of anharmonic XAFS spectra $\chi(k,T)$ at 295 K, 500 K and 700 K. These spectra are shifted and damped as the temperature increases from 295 K to 700 K due to anharmonic contributions. Figs. 4 demonstrate Fourier transform magnitudes of XAFS spectra calculated using the present theory for (a) $T = 295$ K and (b) $T = 700$ K.

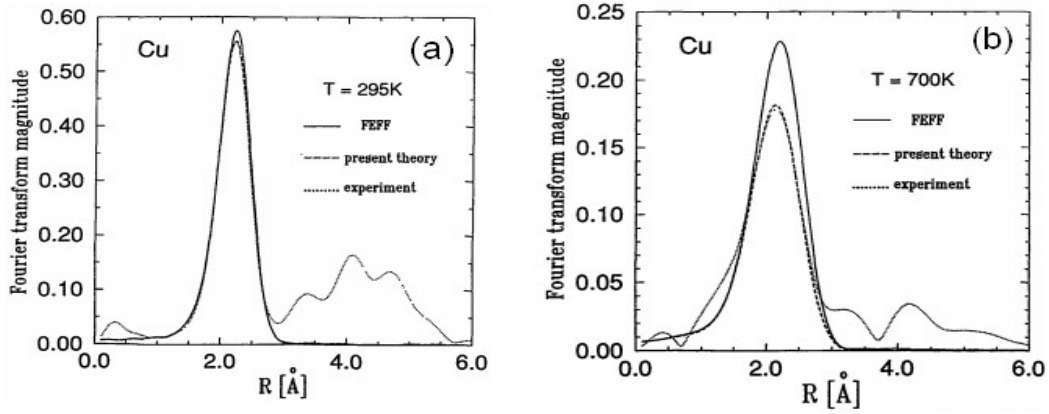


Fig. 4. Fourier transform magnitudes of XAFS spectra of Cu for (a) $T = 295$ K and (b) $T = 700$ K calculated using the present theory compared to the experimental values measured at HASYLAB (DESY, Germany) and to those calculated by FEFF code [8].

II.4. Anharmonic correlated Einstein model [22–27]

II.4.1. Development of anharmonic effective potential procedure [22]

In order to overcome the limitations of single-pair (SP) potential [6, 7] the anharmonic effective potential (AEP) method has developed for which AEP is expanded up to the third order as

$$V_{\text{eff}}(x) \approx \frac{1}{2}k_{\text{eff}}x^2 + k_{3\text{eff}}x^3, \quad x = r - r_0, \quad (47)$$

where k_{eff} is the effective local force constant and k_{3eff} is the cubic anharmonic parameter giving an asymmetry of the AEP, r and r_0 are the instantaneous and equilibrium distances between absorber and backscatter atoms, respectively. Here, k_{eff} and k_{3eff} are specified based on an Einstein potential or an AFP derived from the oscillation of a single pair of atoms with masses M_1 and M_2 (e.g., absorber and backscatter) in a given system. Their oscillation is influenced by their nearest neighbors. In the center-of-mass frame of this bond it is given by

$$V_{eff}(x) = V(x) + \sum_{i=1,2} \sum_{j \neq i} V \left(\frac{\mu}{M_i} x \hat{\mathbf{R}}_{12} \cdot \hat{\mathbf{R}}_{ij} \right), \quad \mu = \frac{M_1 M_2}{M_1 + M_2}, \quad (48)$$

where μ is reduced mass of absorber and backscatter atoms, and $\hat{\mathbf{R}}$ is unit vector; the sum i is over absorber ($i = 1$) and backscatter ($i = 2$), and the sum j is over all their near neighbors, excluding the absorber and backscatter themselves, whose contributions are described by the term $V(x)$.

II.4.2. Deriving analytical expressions of XAFS cumulants in ACEM [22]

The derivation of XAFS cumulants in ACEM is based on quantum statistical theory [58] and the parameters of the AEP, as well as an averaging procedure using the canonical partition function Z and statistical density matrix ρ , e.g.,

$$\langle y^m \rangle = \frac{1}{Z} Tr(\rho y^m), \quad m = 1, 2, 3, \dots \quad (49)$$

Atomic vibrations are quantized in terms of phonons, and anharmonicity is the result of phonon-phonon interaction, that is why we express y in terms of the annihilation and creation operators, \hat{a} and \hat{a}^+ , respectively

$$y \equiv a_0 (\hat{a} + \hat{a}^+), \quad a_0 = \sqrt{\frac{\hbar \omega_E}{10D\alpha^2}}, \quad (50)$$

as well as use the harmonic oscillator state $|n\rangle$ as the eigenstate with the eigenvalue $E_n = n\hbar\omega_E$ for n being the phonon number, ignoring the zero-point energy for convenience.

Due to weak anharmonicity in XAFS, the canonical partition function in Eq. (49) can be expressed as

$$Z \cong Z_0 = \sum_n e^{-n\beta\hbar\omega_E} = \sum_{n=0}^{\infty} z^n = \frac{1}{1-z}, \quad z = \exp(-\theta_E/T), \quad (51)$$

where the correlated Einstein frequency ω_E and temperature θ_E are given by

$$\omega_E = \sqrt{\frac{10D\alpha^2}{M}}, \quad \theta_E = \frac{\hbar\omega_E}{k_B}, \quad (52)$$

M is the atomic mass and k_B is Boltzmann constant.

Consequently, the expressions have resulted for the first cumulant $\sigma^{(1)}$, second cumulant σ^2 , third cumulant $\sigma^{(3)}$ and thermal expansion coefficient α_T describing net thermal expansion, MSRD, mean cubic relative displacement (MCRD), respectively, as

$$\sigma^{(1)}(T) = a = \sigma_0^{(1)} \frac{1+z(T)}{1-z(T)} = \frac{\sigma_0^{(1)}}{\sigma_0^2} \sigma^2(T), \quad \sigma_0^{(1)} = \frac{3\alpha}{4} \sigma_0^2, \quad (53)$$

$$\sigma^2(T) = \langle y^2 \rangle = \sigma_0^2 \frac{1+z(T)}{1-z(T)}, \quad \sigma_0^2 = \frac{\hbar\omega_E}{10D\alpha^2}, \quad (54)$$

$$\sigma^{(3)}(T) = \langle y^3 \rangle = \sigma_0^{(3)} \frac{3(\sigma^2)^2 - 2(\sigma_0^2)^2}{(\sigma_0^2)^2}, \quad \sigma_0^{(3)} = \frac{\alpha}{2} (\sigma_0^2)^2, \quad (55)$$

$$\frac{\sigma^{(1)}\sigma^2}{\sigma^{(3)}} = \frac{1}{2 - (4/3)(\sigma_0^2/\sigma^2)^2}, \quad (56)$$

$$\alpha_T(T) = \frac{1}{r} \frac{da}{dT} = \alpha_T^0 \left(\frac{5D\alpha^2}{k_B T} \right)^2 \left[1 - (\sigma_0^2/\sigma^2)^2 \right], \quad \alpha_T^0 = \frac{3k_B}{20D\alpha r}. \quad (57)$$

II.4.3. Numerical results and discussions

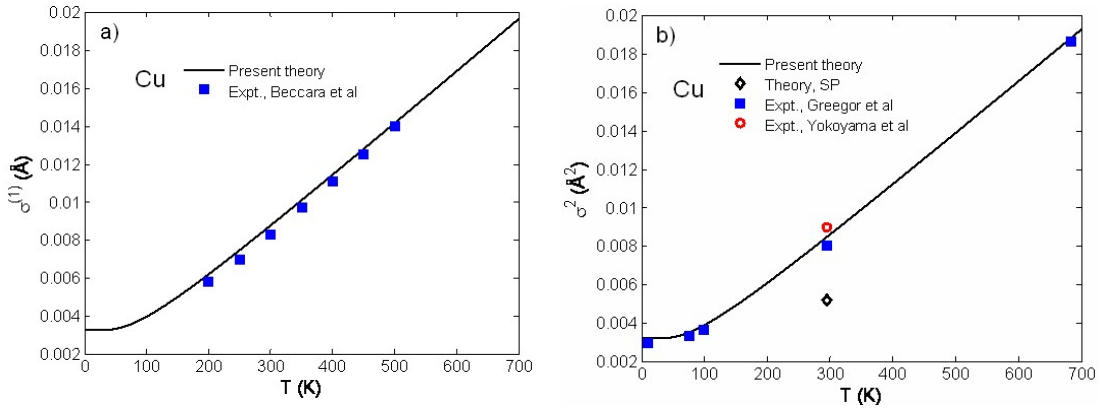


Fig. 5. Temperature dependence of (a) first cumulant $\sigma^{(1)}(T)$ and (b) second cumulant $\sigma^2(T)$ of Cu calculated using the present theory compared to the experimental values [59–61]. The result of $\sigma^2(T)$ at 295 K calculated by SP potential is also presented for comparison.

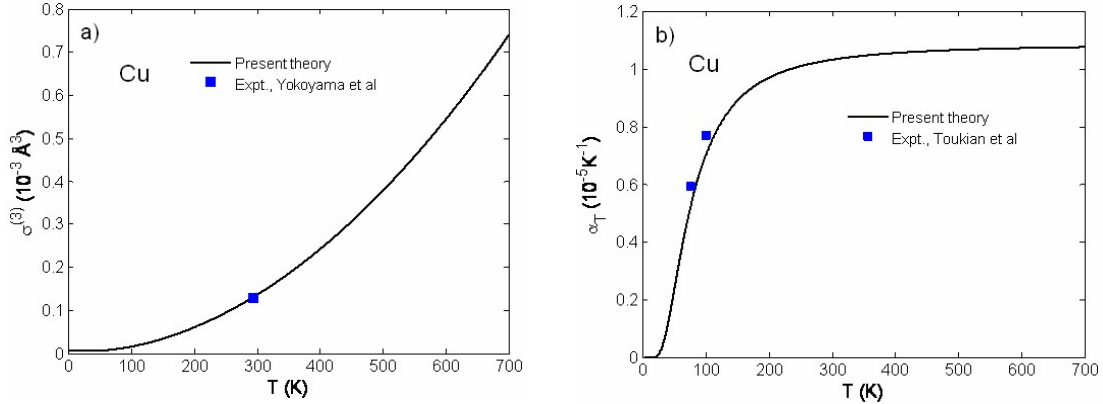


Fig. 6. Temperature dependence of (a) third cumulant $\sigma^{(3)}(T)$ and (b) thermal expansion coefficient $\alpha_T(T)$ of Cu calculated using the present theory compared to the experimental values [61] for the third cumulant and [62] for the thermal expansion coefficient.

Hence, the above figures illustrate good agreement of the results calculated using the present theory (ACEM) with the experimental values, as well its advantage compared to the SPP method.

II.5. Anharmonic XAFS theory [23–25]

II.5.1. Derivation of anharmonic XAFS theory based on ACEM

The theory derived in Section 3.3 is limited due to using T_0 as a fitting parameter. In order to overcome these limitations, the anharmonic XAFS theory is derived based on the ACEM whose expression based on the cumulant expansion approach [5] is given by

$$\chi(k, T) = \sum_j \frac{S_0^2 N_j}{k R_j^2} F_j(k) F_A(k, T) e^{-(2k^2 \sigma^2(T) + 2R_j/\lambda(k))} \sin\left(2kR_j + \Phi_j(k) + \Phi_A^j(k, T)\right), \quad (58)$$

which contains anharmonic contributions to amplitude by factor F_A and to phase Φ_A as

$$F_A(k, T) = \exp\left[-2k^2 \sigma_A^2(T)\right], \quad (59)$$

$$\Phi_A^j(k, T) = 2k \left[\sigma^{(1)}(T) - 2\sigma_A^2(T) \left(\frac{1}{R_j} - \frac{1}{\lambda(k)} \right) - \frac{2}{3} \sigma^{(3)}(T) k^2 \right],$$

$$\sigma_A^2(T) = \beta_A(T) [\sigma^2(T) - \sigma_0^2],$$

$$\beta_A(T) = \frac{9\alpha^2}{8} \sigma^2(T) \left[1 + \frac{3\alpha}{4R} \sigma^2(T) \left(1 + \frac{3\alpha}{4R} \sigma^2(T) \right) \right]. \quad (60)$$

II.5.2. Numerical results and discussions

Note that above Figs. 7-9 illustrate good agreement of the numerical results of hcp crystals Zn and Cd calculated using the expressions derived above and their Morse potential parameters [63] with the experimental values measured at HASYLAB (DESY, Germany).

Hence, the derived anharmonic XAFS theory based on the ACEM has successfully simplified the complicated quantum many-body task into the one of one-dimensional model with taking many-body effects into account based on including contributions of nearest neighbors of absorber and scattering atoms (FSNNCA). It avoids complicated full lattice dynamical calculations yet provides good agreement of theoretical results with experiment.

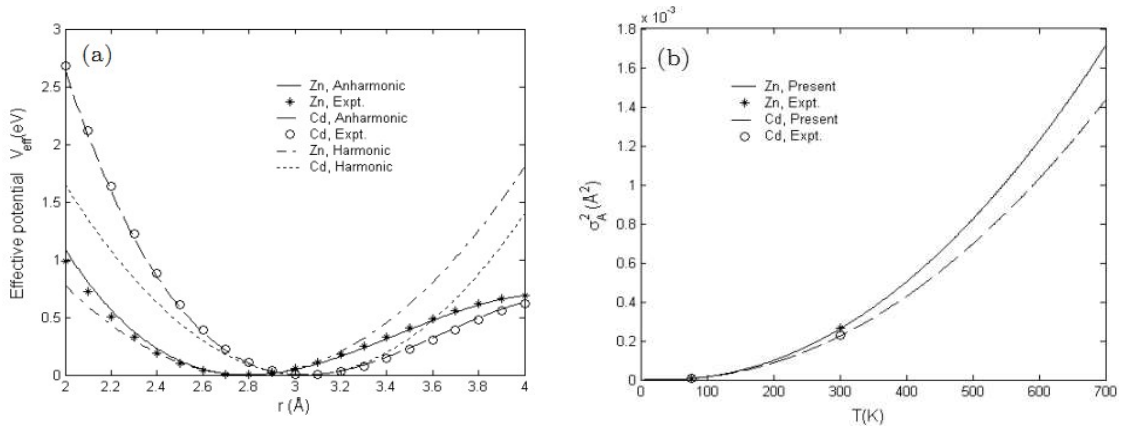


Fig. 7. (a) Anharmonic effective Potentials V_{eff} (eV), their harmonic terms, and (b) $\sigma_A^2(T)$ of Zn and Cd compared to the experimental values measured at HASYLAB (DESY, Germany).

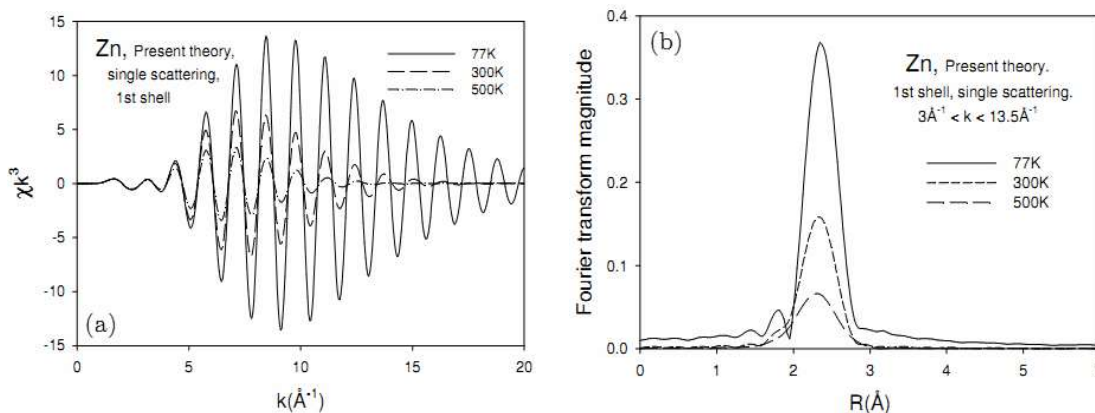


Fig. 8. (a) XAFS spectra at 77 K, 300 K, 500 K and (b) their Fourier transform magnitudes of Zn calculated using the present theory.

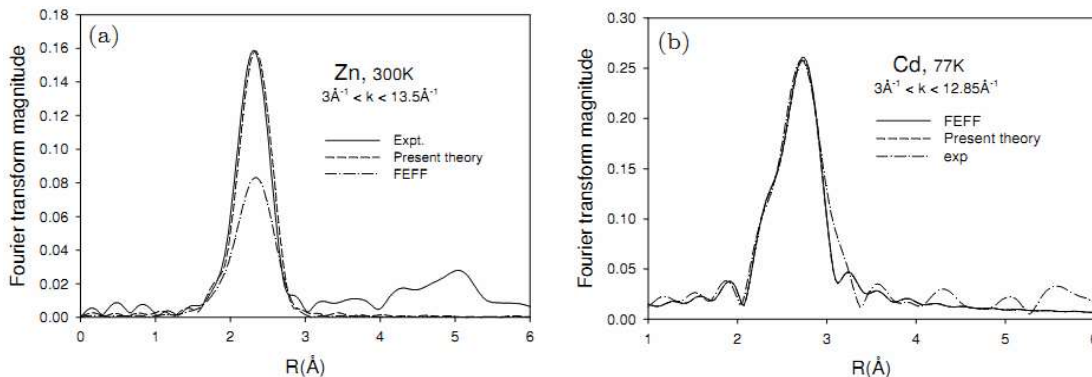


Fig. 9. Fourier transform magnitudes of XAFS spectra of (a) Zn at 300 K and (b) Cd at 77 K calculated using the present anharmonic theory compared to those calculated by FEFF-code [8] and to the experimental values measured at HASYLAB (DESY, Germany).

II.6. ACEM method for calculating XAFS local force constants of doping materials compared to Mössbauer studies [26]

Mössbauer is an exact well-known method. The Mössbauer effect has been used extensively to measure the ratio r_X of host-host to dopant-host local force constants for dilute alloys. XAFS can also be related to local force constant, unlike the Mössbauer effect is applied only to the dopant atomic species for which Mössbauer is active. *“Temperature dependent XAFS results can be related to local force constants using the correlated Einstein model of Hung and Rehr, this is a simplified approach that considers a single pair of vibrating atoms in a small cluster and assumes a Morse potential. . . The model of Van Hung and Rehr assumes central force only, and assumes that only near-neighbor forces are significant....The Mössbauer theory of Mannheim also*

assumes the validity of near-neighbor central forces...” [26,64]. Based on this similarity between the present theory and Mössbauer theory of Mannheim and analyzing the atomic distributions we obtain the desired result for the host (H) substance with atomic mass M_H doped by the doping (D) atoms with the mass M_D

$$r_X = 2 \left[\theta_{E(H)} / \theta_{E(HD)} \right]^2 (M_H / 2\mu) (3C_2 + 1) / \left\{ 5 - 6C_1 \left[\theta_{E(H)} / \theta_{E(HD)} \right]^2 (M_H / 2\mu) \right\}, \quad (61)$$

$$C_1 = [M_D / (M_H + M_D)]^2, \quad C_2 = [M_H / (M_H + M_D)]^2, \quad \mu = \frac{M_H M_D}{M_H + M_D}, \quad (62)$$

where $\theta_{E(H)}$, $\theta_{E(HD)}$ are Einstein temperatures of the host and doping material, respectively.

The XAFS results using the present theory agree well with the Mössbauer theory of Mannheim so that “At present the best theoretical framework with which the experimentalists can relate force constants to temperature-dependent XAFS is Hung and Rehr theory”, as it was mentioned in [26,64].

II.7. ACEM for studying impurity effects [26,27]

II.7.1. Impurity effects in Debye-Waller factors of bcc crystals based on ACEM

Actually, the ACEM for impure materials is derived beginning from development of anharmonic effective potential for impure bcc crystals in the form

$$\begin{aligned} V_{eff}(x) &\cong \frac{1}{2} k_{eff}^{HD} x^2 + k_3^{HD} x^3 + \dots \\ &= V_{HD}(x) + \sum_{j \neq i} V_{HD} \left(\frac{\mu}{M_i} x \hat{\mathbf{R}}_{12} \cdot \hat{\mathbf{R}}_{ij} \right) \\ &= V_{HD}(x) + V_{HD}(\kappa x) + 3V_{HD} \left(\kappa \frac{x}{3} \right) + 3V_{HD} \left(-\kappa \frac{x}{3} \right) \\ &\quad + V_{HH} \left(\frac{x}{2} \right) + 3V_{HH} \left(\frac{x}{6} \right) + 3V_{HH} \left(-\frac{x}{6} \right), \\ \mu &= \frac{M_H M_D}{M_H + M_D}, \quad \kappa = \frac{M_H}{M_H + M_D}, \end{aligned} \quad (63)$$

where μ is reduced mass, $\hat{\mathbf{R}}$ is bond unit vector, the sum i is over all first shell near neighbors of absorber and the sum j is over all those of backscatter. The first term on the right of Eqs. (63) concerns only absorber and backscatter and the other ones describe the lattice contributions to the oscillation between absorber and backscattering atoms based on that the many-body effects are taken into account in the present one-dimensional model. Here, the first equation of Eqs. (63) is valid for all crystal structures and the second one is for bcc crystals.

Here, the effective local force constant k_{eff} and cubic anharmonic parameter k_{3eff} of impure materials have resulted as

$$\begin{aligned} k_{eff} &= 2 \left[D_{HD} \alpha_{HD}^2 (1 + 5\kappa^2/3) + 5D_H \alpha_H^2 / 12 \right], \\ k_{3eff} &= -D_{HD} \alpha_{HD}^3 (1/2 + \kappa^3) + D_H \alpha_H^3 / 8. \end{aligned} \quad (64)$$

Using k_{eff} the correlated Einstein frequency ω_E and temperature θ_E of impure material are given by

$$\omega_E = \sqrt{k_{eff}/\mu} = \{2 [D_{HD}\alpha_{HD}^2 (1 + 5\kappa^2/3) + 5D_H\alpha_H^2/12] / \mu\}^{1/2}, \quad (65)$$

$$\theta_E = \hbar\omega_E/k_B = \hbar \{2 [D_{HD}\alpha_{HD}^2 (1 + 5\kappa^2/3) + 5D_H\alpha_H^2/12] / \mu\}^{1/2} / k_B, \quad (66)$$

Consequently, the expressions have resulted for the first cumulant $\sigma^{(1)}$, second cumulant σ^2 , third cumulant $\sigma^{(3)}$ and thermal expansion coefficient α_T for impure materials as

$$\sigma^{(1)}(T) = a = \sigma_0^{(1)} \frac{1+z(T)}{1-z(T)} = \frac{\sigma_0^{(1)}}{\sigma_0^2} \sigma^2(T), \quad \sigma_0^{(1)} = -\frac{3k_{3eff}}{k_{eff}} \sigma_0^2, \quad z = \exp(\theta_E/T), \quad (67)$$

$$\sigma^2(T) = \sigma_0^2 \frac{1+z(T)}{1-z(T)}, \quad \sigma_0^2 = \frac{\hbar\omega_E}{2k_{eff}} = \frac{\hbar}{2 \{2\mu [D_{HD}\alpha_{HD}^2 (1 + 5\kappa^2/3) + 5D_H\alpha_H^2/12]\}^{1/2}}, \quad (68)$$

$$\sigma^{(3)}(T) = \langle y^3 \rangle = \sigma_0^{(3)} [3(\sigma^2(T)/\sigma_0^2)^2 - 2], \quad \sigma_0^{(3)} = -\frac{2k_{3eff}}{k_{eff}} (\sigma_0^2)^2, \quad (69)$$

$$\alpha_T(T) = \frac{1}{r} \frac{da}{dT} = \alpha_T^0 \frac{(\sigma^2(T))^2 - (\sigma_0^2)^2}{T^2}, \quad \alpha_T^0 = -\frac{3k_{3eff}}{k_B r}, \quad (70)$$

where $\sigma_0^{(1)}$, σ_0^2 , $\sigma_0^{(3)}$ are zero-point energy contributions to the cumulants $\sigma^{(1)}(T)$, $\sigma^2(T)$, $\sigma^{(3)}(T)$, respectively, and α_T^0 is the constant value which the $\alpha_T(T)$ approaches at high-temperatures. They include the impurity effects because of containing the data of doping atom. Here, Morse parameters D_{HD} , α_{HD} of impure materials are taken from those of pure elements.

II.7.2. Numerical results and discussions

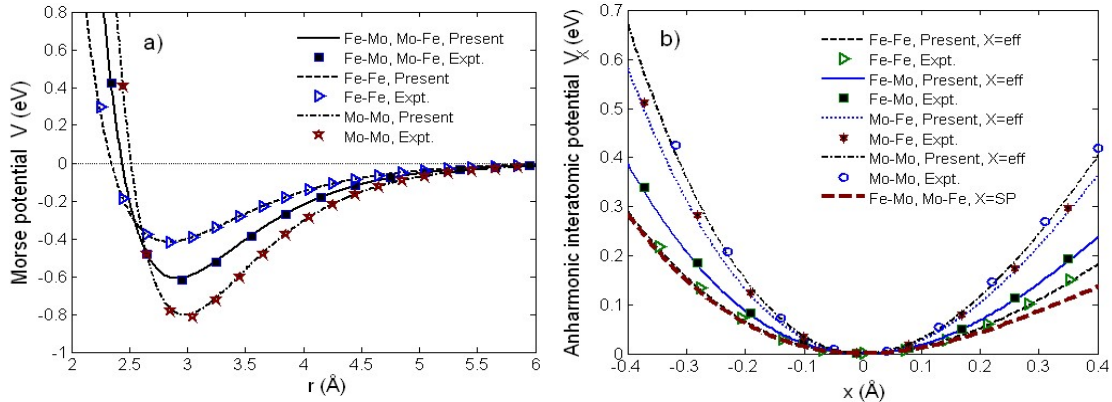


Fig. 10. (a) Morse potentials for Fe doped by Mo (Fe-Mo) and inversely for Mo doped by Fe (Mo-Fe) calculated from those of pure Fe and Mo, i.e., Fe-Fe, Mo-Mo, and (b) their anharmonic interatomic effective $V_{eff}(x)$ and single-pair $V_{SP}(x)$ potentials compared to experiment of the pure crystals [65] and of those for (Fe-Mo) and (Mo-Fe) obtained from MMP [65] of Fe, Mo.

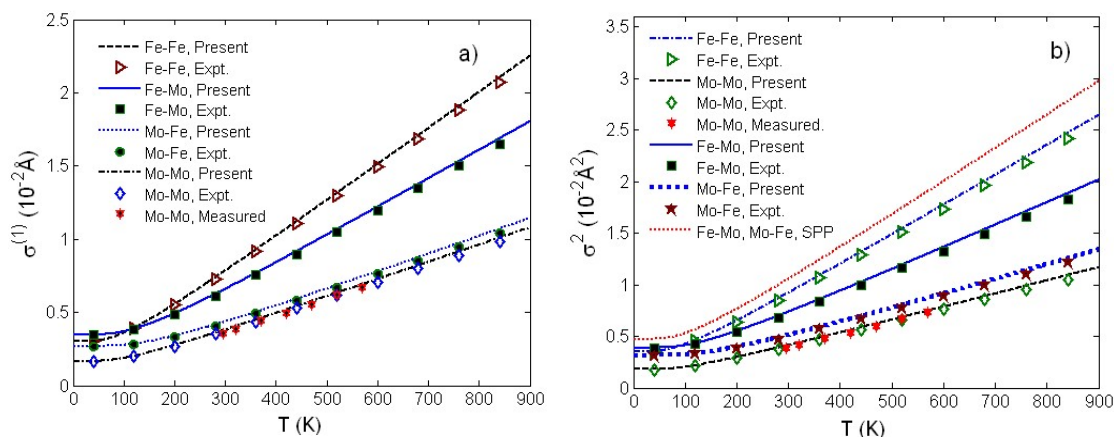


Fig. 11. Temperature dependence of (a) first cumulant $\sigma^{(1)}(T)$ and (b) second cumulant or MSRD $\sigma^2(T)$ of Fe doped by Mo (Fe-Mo) and inversely of Mo doped by Fe (Mo-Fe), and for pure Fe (Fe-Fe) and Mo (Mo-Mo) calculated using the present theory compared to experiment (Expt.) obtained from MMP [65] and to the measured values (Measured) [65] for pure Mo (Mo-Mo).

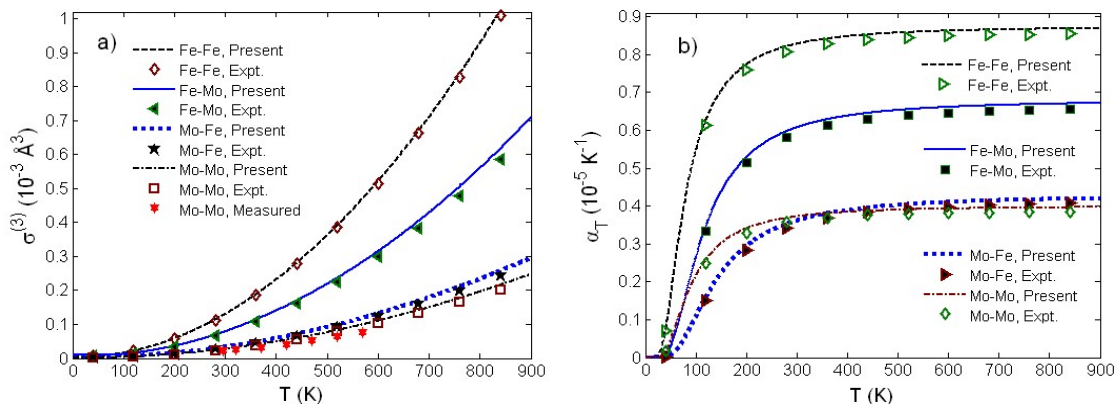


Fig. 12. Temperature dependence of (a) third cumulant $\sigma^{(3)}(T)$ and (b) thermal expansion coefficient $\alpha_T(T)$ of Fe doped by Mo (Fe-Mo) or inversely of Mo doped by Fe (Mo-Fe) and of pure Fe, Mo, i.e., Fe-Fe, Mo-Mo calculated using the present theory compared to experiment obtained from the MMP [65]. Here the results of $\sigma^{(3)}(T)$ are compared to the measured values (Measured) [65] for pure Mo (Mo-Mo) at different temperatures.

Hence, Figs. 10–12 illustrate numerical results of Morse potentials, interatomic potentials, as well as temperature-dependent first, second, third cumulants and thermal expansion coefficient of several bcc crystals doped by atoms of other bcc crystals calculated using the present theory and Morse potentials [57]. They agree well with the experimental values. Moreover, the values of anharmonic effective potentials, cumulants and thermal expansion coefficients are the same for

two inverse doping processes if the SPP is used for calculation (Figs. 10b and 11b). This shows the advantage of the present theory and the limitations of SPP in describing these doping processes.

II.8. Advanced method for theoretical and experimental XAFS studies [28–31]

II.8.1. Creation of advanced method for theoretical and experimental XAFS studies

Main development in the advanced method is presenting all considered quantities such as the first cumulant $\sigma^{(1)}$, second cumulant σ^2 , third cumulant $\sigma^{(3)}$ and thermal expansion coefficient α_T in terms of second cumulant or MSRD

$$\sigma^2(T) = \sigma_0^2 \frac{1+z(T)}{1-z(T)}, \quad \sigma_0^2 = \frac{\hbar\omega_E}{10D\alpha^2}, \quad z(T) = \exp(-\theta_E/T). \quad (71)$$

$$\sigma^{(1)}(T) = a = \sigma_0^{(1)} \frac{1+z(T)}{1-z(T)} = \frac{\sigma_0^{(1)}}{\sigma_0^2} \sigma^2(T), \quad \sigma_0^{(1)} = \frac{3\alpha}{4} \sigma_0^2, \quad (72)$$

$$\sigma^{(3)}(T) = \sigma_0^{(3)} \left[3 \left(\frac{\sigma^2(T)}{\sigma_0^2} \right)^2 - 2 \right], \quad \sigma_0^{(3)} = \frac{\alpha}{2} (\sigma_0^2)^2, \quad (73)$$

$$\alpha_T(T) = \frac{1}{r} \frac{da}{dT} = \alpha_T^0 \frac{(\sigma^2(T))^2 - (\sigma_0^2)^2}{T^2}, \quad \alpha_T^0 = \frac{15D\alpha^3}{4k_B r}, \quad (74)$$

where $\sigma_0^{(1)}$, σ_0^2 , $\sigma_0^{(3)}$ are zero-point energy contributions to the cumulants $\sigma^{(1)}(T)$, $\sigma^2(T)$, $\sigma^{(3)}(T)$, respectively, and α_T^0 is the constant value which the α_T approaches at high-temperatures.

Note that the second cumulant given by Eq. (71) is harmonic while the experimental data always include the anharmonic effects. That is why the total second cumulant σ_{tot}^2 is introduced as

$$\sigma_{tot}^2(T) = \sigma^2(T) + \sigma_A^2(T), \quad \sigma_A^2(T) = \beta_A(T) [\sigma^2(T) - \sigma_0^2], \quad (75)$$

which involves an anharmonic contribution σ_A^2 containing the anharmonic factor

$$\beta_A(T) = \frac{9\alpha^2}{8} \sigma^2(T) \left[1 + \frac{3\alpha}{4R} \sigma^2(T) \left(1 + \frac{3\alpha}{4R} \sigma^2(T) \right) \right]. \quad (76)$$

In this advanced method the same presentation in terms of second cumulant is performed for XAFS

$$\chi(k, T) = \sum_j \frac{S_0^2 N_j}{k R_j^2} F_j(k) F_A(k, T) e^{-(2k^2 \sigma^2(T) + 2R_j/\lambda(k))} \sin \left(2k R_j + \Phi_j(k) + \Phi_A^j(k, T) \right), \quad (77)$$

which contains the anharmonic contributions to amplitude $F_A(k)$ and phase $\Phi_A(k, T)$ of XAFS as

$$F_A(k, T) = \exp \left[-2k^2 \sigma_A^2(T) \right], \quad (78)$$

$$\Phi_A^j(k, T) = 2k \left[\sigma^{(1)}(T) - 2\sigma_A^2(T) \left(\frac{1}{R_j} - \frac{1}{\lambda(k)} \right) - \frac{2}{3} \sigma^{(3)}(T) k^2 \right].$$

Note that the present advanced method has the advantage of providing all theoretical or experimental considered quantities based only the calculated or measured second cumulants.

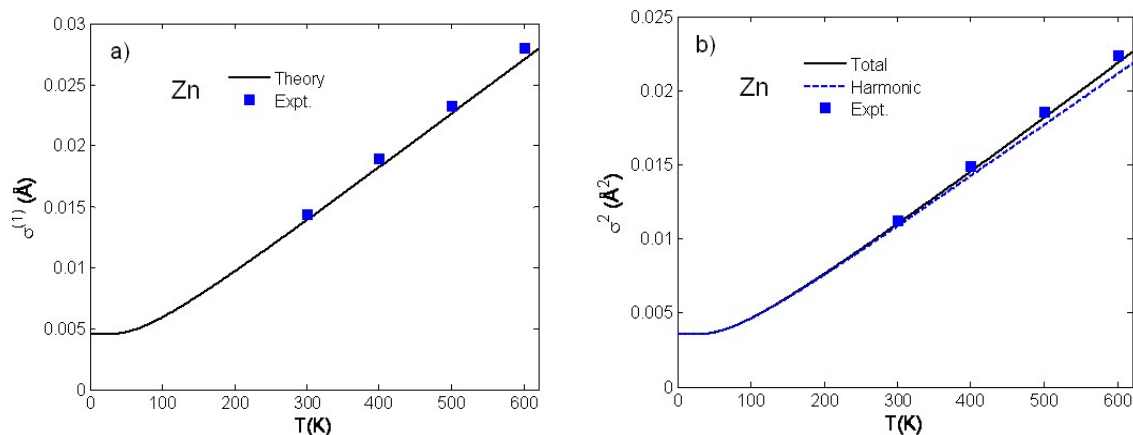


Fig. 13. Temperature dependence of (a) first cumulant $\sigma^{(1)}(T)$ and (b) total and harmonic second cumulants $\sigma_{tot}^2(T)$ and $\sigma^2(T)$, respectively, of Zn calculated using the present theory compared to the experimental values at 300 K, 400 K, 500 K and 600 K.

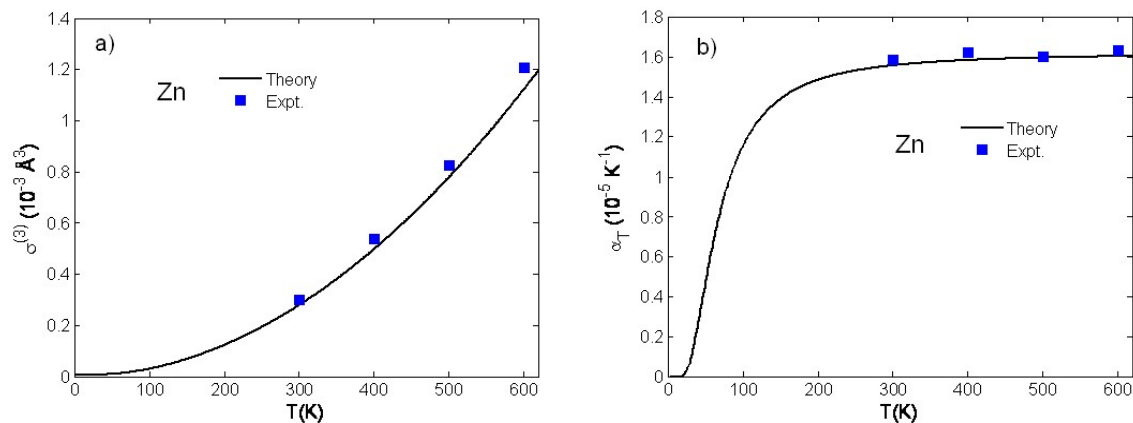


Fig. 14. Temperature dependence of (a) third cumulant $\sigma^{(3)}(T)$ and (b) thermal expansion coefficient $\alpha_T(T)$ of Zn calculated using the present theory compared to the experimental values at 300 K, 400 K, 500 K and 600 K.

II.8.2. Numerical, experimental results and discussions

Hence, the above Figs. 13–15 illustrate numerical results for cumulants and XAFS of Zn calculated using the present theory and Morse potential [63]. They agree well with the experimental values at 300 K, 400 K, 500 K measured at the Beamline BL8 (SLRI, Thailand).

II.9. ACEM for studying isotopes and isotopic effects [32]

II.9.1. Derivation of ACEM for isotopes and isotopic effects

ACEM for isotopes and isotopic effects includes the same analytical expressions for cumulants and XAFS presented in Sections 4 and 5 which are not written here again, but in these

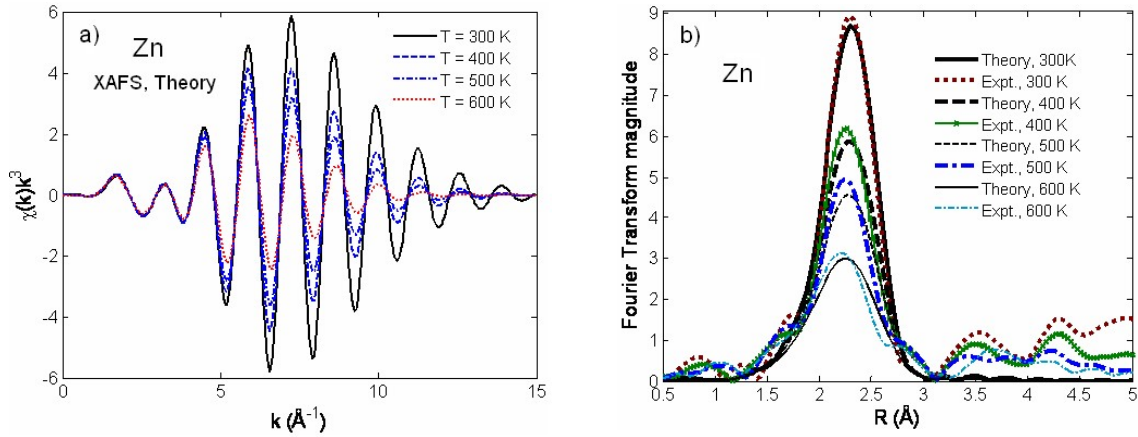


Fig. 15. (a) XAFS spectra of Zn at 300 K, 400 K, 500 K, 600 K calculated using the present theory and (b) Fourier transform magnitudes of these spectra compared to those measured at the Beamline BL8 (SLRI, Thailand).

analytical expressions the parameter m for atomic mass is now a variable describing different isotopes. The purpose of this model is to describe the cumulants for isotopes describing the thermodynamic properties of isotopes themselves and the isotopic effects expressed by the difference of two isotopes.

II.9.2. Numerical results and discussions

Numerical calculations are carried out for Ni and its isotopes ^{68}Ni , ^{64}Ni , ^{50}Ni , ^{40}Ni using the present theory and their Morse potentials [57].

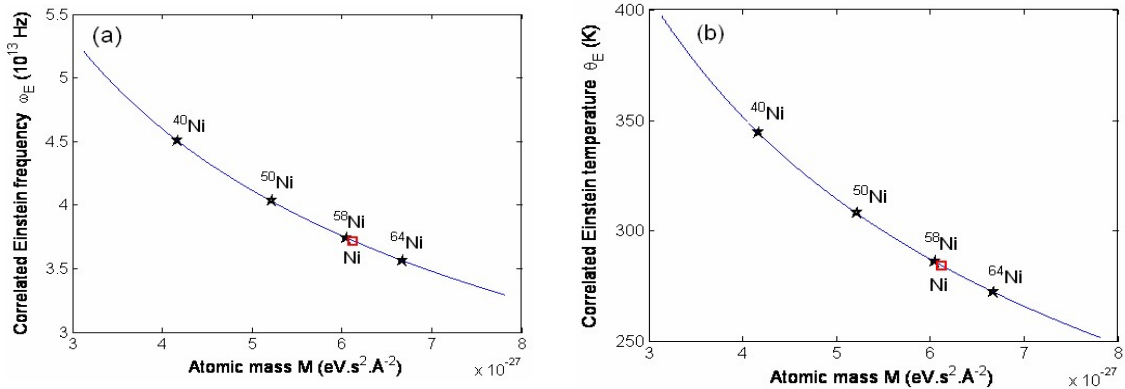


Fig. 16. Dependence of correlated Einstein (a) frequencies ω_E and (b) temperatures θ_E of Ni and its isotopes ^{68}Ni , ^{64}Ni , ^{50}Ni , ^{40}Ni on their atomic mass M calculated using the present theory.

Hence, the above figures describe the isotopic effects for correlated Einstein frequencies ω_E and temperatures θ_E , for second cumulant $\sigma^2(T)$ and for XAFS spectra and their Fourier transform magnitudes of Ni and its isotopes using the present theory and Morse potential [57].

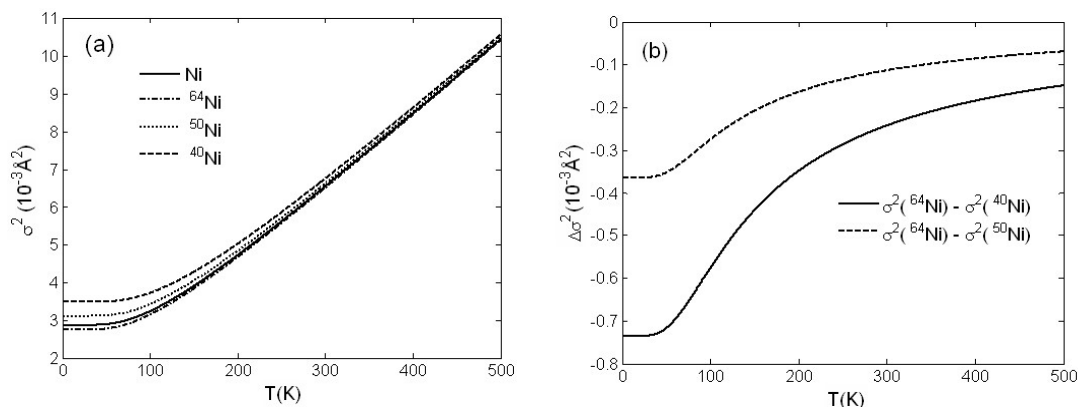


Fig. 17. Temperature-dependent (a) second cumulant $\sigma^2(T)$ of Ni and its isotopes ^{64}Ni , ^{58}Ni , ^{40}Ni and (b) differences $\Delta\sigma^2(T)$ for two different isotopes, e.g., $\sigma^2(^{64}\text{Ni}) - \sigma^2(^{40}\text{Ni})$ and $\sigma^2(^{64}\text{Ni}) - \sigma^2(^{50}\text{Ni})$ calculated using the present theory.

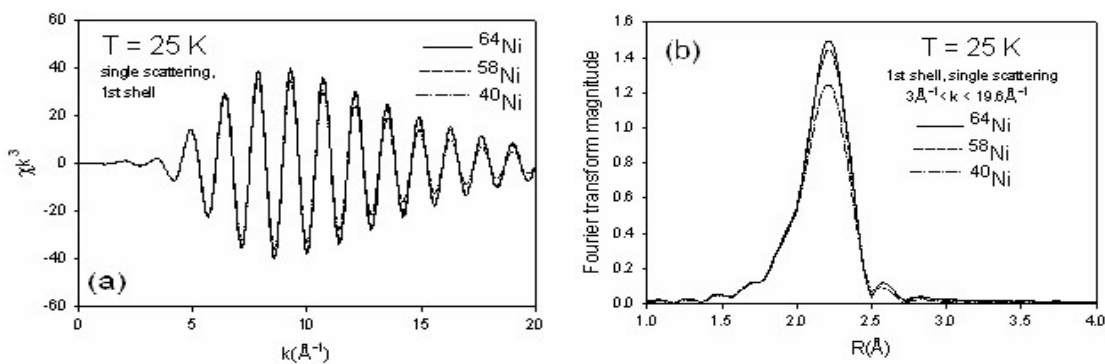


Fig. 18. (a) EXAFS spectra and (b) their Fourier transform magnitudes of isotopes ^{64}Ni , ^{58}Ni , ^{40}Ni at $T = 25\text{ K}$ calculated using the present theory.

These results are found to be in good similarity to those obtained in the XAFS experimental results of isotopes ^{76}Ge and ^{70}Ge [66]. The isotopic effects are significant at low-temperatures and decrease as the temperature increases so that they can be studied only by quantum theory.

II.10. Classical ACEM [33,34]

II.10.1. High-order expanded Debye-Waller of fcc crystals based on classical ACEM [33]

Classical theory has the advantage of simplicity and including the dominant anharmonicity at high-temperatures. The present classical ACEM is derived based on classical statistical theory. Here, the AEP and Debye-Waller factor (DWF) presented in terms of cumulant expansion are

expanded up to the fourth order. These expressions have resulted for the AEP as

$$V_{eff}(x) = V(x) + \sum_{i=1,2} \sum_{j \neq i} V \left(\frac{\mu}{M_i} x \hat{\mathbf{R}}_{12} \cdot \hat{\mathbf{R}}_{ij} \right) = V(x) + 2V \left(-\frac{x}{2} \right) + 8V \left(-\frac{x}{4} \right) + 8V \left(\frac{x}{4} \right), \quad (79)$$

as well as for four first XAFS cumulants describing DWF

$$\sigma^{(1)} = \frac{3}{4} \alpha \sigma^2, \quad \sigma^2 = \frac{k_B T}{5D\alpha^2}, \quad \sigma^{(3)} = \frac{3}{2} \alpha (\sigma^2)^2, \quad \sigma^{(4)} = \frac{137}{40} \alpha^2 (\sigma^2)^3. \quad (80)$$

Note that the total second cumulant or MSRD is described as

$$\sigma_{tot}^2(T) = \sigma^2(T) + \sigma_A^2(T), \quad \sigma_A^2(T) = \beta(T) \sigma^2(T), \quad \beta(T) = \frac{9\alpha^2}{8} \sigma^2 \left[1 + \frac{3\alpha}{4R} \sigma^2 \left(1 + \frac{3\alpha}{4R} \sigma^2 \right) \right]. \quad (81)$$

II.10.2. Numerical results and discussions

The expressions derived above are used for numerical calculations of cumulants of Zn and Cd using their Morse potential parameters [57]. Some results are illustrated bellows showing their good agreement at 300 K and disagreement at 77 K with the experimental values [25] due to the absence of zero-point vibrations at low-temperatures.

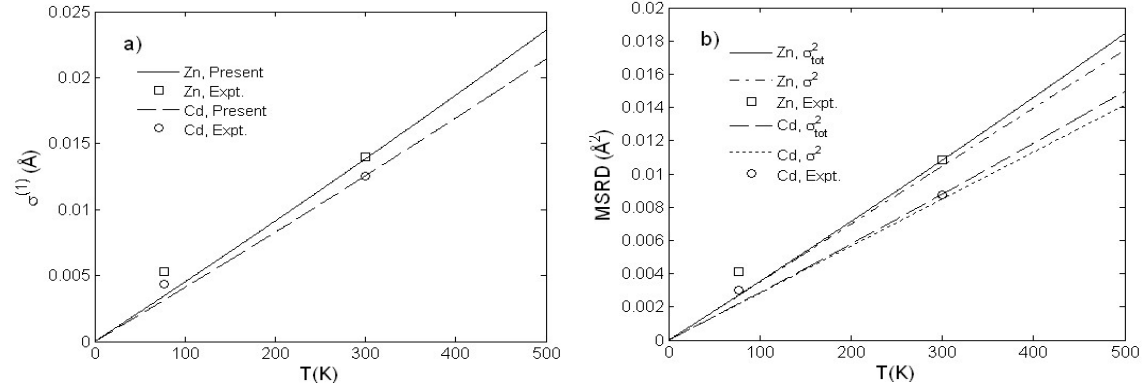


Fig. 19. Temperature dependence of (a) first cumulant $\sigma^{(1)}(T)$, and (b) second cumulant $\sigma^2(T)$ and total MSRD $\sigma_{tot}^2(T)$, calculated using the present theory for Zn and Cd compared to the experimental values at 77 K and 300 K [25].

II.11. Pressure-dependent ACEM [35]

II.11.1. Derivation of pressure-dependent ACEM

The main purpose of this model is to obtain all considered quantities having pressure dependence. Firstly, the pressure-dependent anharmonic effective potential (AEP) has resulted for the case under pressure P the interatomic distance is changed by $\Delta r(P)$

$$V_{eff}(P) \cong \frac{1}{2} k_{eff} (\Delta r(P))^2 + k_3 (\Delta r(P))^3 + k_4 (\Delta r(P))^4, \quad \Delta r(P) = r(P) - r(0), \quad (82)$$

where $\Delta r(P)$ is pressure-induced change of interatomic distance, k_{eff} is effective spring constant, k_3 and k_4 are cubic and quartic anharmonic parameters, giving an asymmetry of the potential.

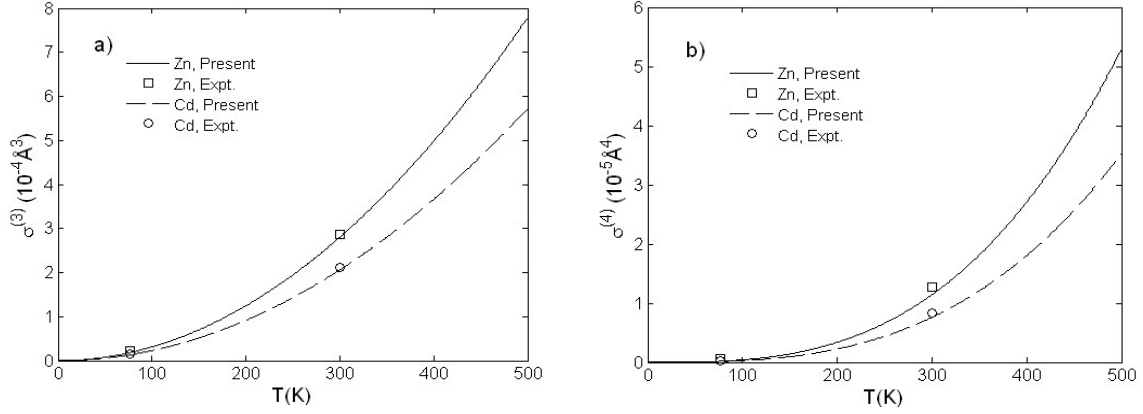


Fig. 20. Temperature dependence of (a) third cumulant $\sigma^{(3)}(T)$ and (b) fourth cumulant $\sigma^{(4)}(T)$, calculated using the present theory for Zn and Cd compared to the experimental values at 77 K and 300 K [25].

These parameters are defined based on an assumption in the center-of-mass frame of single-bond pair of absorber with mass M_1 and back-scatterer with mass M_2 as

$$V_{\text{eff}}(P) = V(P) + \sum_{i=1,2} \sum_{j \neq i} V \left(\frac{\mu}{M_i} \Delta r(P) \hat{\mathbf{R}}_{12} \cdot \hat{\mathbf{R}}_{ij} \right), \quad \mu = \frac{M_1 M_2}{M_1 + M_2}, \quad (83)$$

where the sum i is over absorber and backscattering atoms, the sum j is over their nearest neighbors, $\hat{\mathbf{R}}_{ij}$ the unit vector along the bond between i th and j th atoms, μ is reduced mass of M_1 and M_2 .

Making use of quantum thermodynamic perturbation theory [58] and above pressure-dependent AEP the analytical expressions for three XAFS cumulants and thermal expansion coefficient as functions of pressure P at a given temperature T have been derived and given by

$$\sigma^{(1)}(P, T) = \sigma_0^{(1)}(P) \frac{1 + z(V(P), T)}{1 - z(V(P), T)} = \frac{3k_3}{k_{\text{eff}}(P)} \sigma^2(P, T), \quad \sigma_0^{(1)}(P) = -\frac{3k_3}{k_{\text{eff}}(P)} \sigma_0^2(P), \quad (84)$$

$$\sigma^2(P, T) = \sigma_0^2(P) \frac{1 + z(P, T)}{1 - z(P, T)}, \quad \sigma_0^2(P) = \frac{\hbar \omega_E(P)}{2k_{\text{eff}}(P)}, \quad z(P, T) = \exp\left(-\frac{\theta_E(P)}{T}\right), \quad (85)$$

$$\sigma^{(3)}(P, T) = \sigma_0^{(3)}(P) \left[3 \left(\sigma^2(P, T) / \sigma_0^2(P) \right)^2 - 2 \right], \quad \sigma_0^{(3)}(P) = -\frac{2k_3}{k_{\text{eff}}(P)} \left(\sigma_0^2(P) \right)^2, \quad (86)$$

$$\alpha_P(P, T) = \alpha_P^0(P) \frac{(\sigma^2(P, T))^2 - (\sigma_0^2(P))^2}{T^2}, \quad \alpha_P^0(P) = -\frac{3k_3}{r(P) k_B}, \quad z(P, T) = \exp\left(-\frac{\theta_E(P)}{T}\right). \quad (87)$$

II.11.2. Numerical results and discussions

Note that the results calculated by the present pressure-dependent ACEM presented in Figs. 21–22 are found to be in good agreement with experiment and with those predicted by other methods.

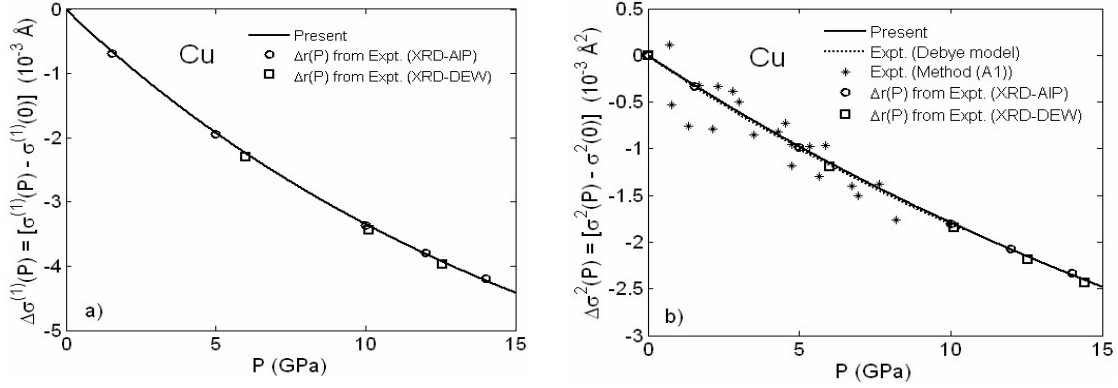


Fig. 21. Pressure dependence of pressure-induced (a) first cumulant change $\Delta\sigma^1(P)$ of Cu calculated by the present theory compared to the experimental values [67] and (b) second cumulant change $\Delta\sigma^2(P)$ of Cu compared to those from Debye model and method (A1) [68].

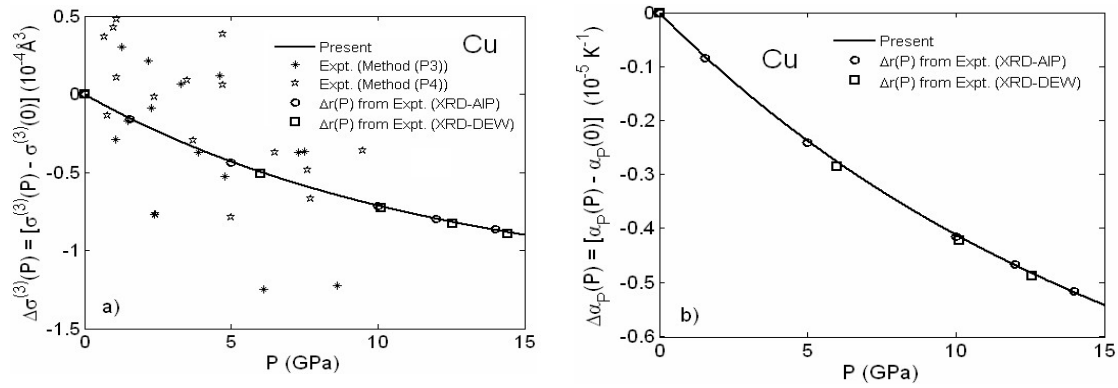


Fig. 22. (a) Pressure dependence of pressure-induced third cumulant change $\Delta\sigma^3(P)$ and (b) $\alpha_p(P)$ of Cu calculated by present theory compared to the experimental results extracted from XAFS by using methods (P3) and (P4) [68] or predicted using $\Delta r(P)$ from XRD (AIP, DEW) experiment [67].

II.12. Anharmonic correlated Debye model (ACDM) [36–46]

II.12.1. Derivation of anharmonic correlated Debye model

The main purpose of the ACDM is to create a model for the calculation and analysis of XAFS DWFs presented in terms of cumulant expansion up to the fourth order including dispersion contributions. The model is characterized by an AEP expanded up to the fourth order

$$V_{eff}(x) \approx \frac{1}{2}k_{eff}x^2 + k_{3eff}x^3 + k_{4eff}x^4, \quad (88)$$

where k_{eff} is effective local force constant, k_{3eff} and k_{4eff} are effective anharmonic parameters giving an asymmetry of the anharmonic effective potential, x is deviation of the instantaneous bond length between two immediate neighboring atoms from its equilibrium.

The dispersion relation included in the ACDM is expressed as

$$\omega(q) = 2\sqrt{\frac{k_{eff}}{M}} \left| \sin\left(\frac{qa}{2}\right) \right|, \quad |q| \leq \frac{\pi}{a}, \quad (89)$$

where q is phonon wave number, M is mass of composite atoms, and a is lattice constant.

Consequently, the analytical expressions of four first temperature-dependent XAFS cumulants $\sigma^{(1)}$, σ^2 , $\sigma^{(3)}$, and $\sigma^{(4)}$ describing DWFs in ACDM have been derived and given by

$$\begin{aligned} \sigma^{(1)} &= \frac{3a\hbar k_{3eff}}{2\pi k_{eff}^2} \int_0^{\pi/a} \omega(q) \frac{1+Z(q)}{1-Z(q)} dq, \quad Z(q) \\ &= \exp(\beta\hbar\omega(q)), \quad \beta = 1/k_B T, \end{aligned} \quad (90)$$

$$\begin{aligned} \sigma^2 = \langle x^2 \rangle &= -\frac{\hbar a}{\pi\sqrt{Mk_{eff}}} \int_0^{\pi/a} \left| \sin\frac{qa}{2} \right| \frac{1+z(q)}{1-z(q)} dq \\ &= -\frac{\hbar a}{2\pi k_{eff}} \int_0^{\pi/a} \omega(q) \frac{1+z(q)}{1-z(q)} dq, \end{aligned} \quad (91)$$

$$\sigma^{(3)} = \frac{3\hbar^2 k_{3eff} a^2}{4\pi^2 k_{eff}^3} \int_0^{\pi/a} dq_1 \int_{-\pi/d}^{\pi/a-q_1} dq_2 F(q_1, q_2), \quad (92)$$

$$\begin{aligned} &F(q_1, q_2) \\ &= \frac{\omega(q_1)\omega(q_2)\omega(q_1+q_2)}{\omega(q_1)+\omega(q_2)+\omega(q_1+q_2)} \\ &\times \left\{ 1 + 6 \frac{\omega(q_1)+\omega(q_2)}{\omega(q_1)+\omega(q_2)-\omega(q_1+q_2)} \frac{e^{\beta\hbar[\omega(q_1)+\omega(q_2)]} - e^{\beta\hbar\omega(q_1+q_2)}}{(e^{\beta\hbar\omega(q_1)}-1)(e^{\beta\hbar\omega(q_2)}-1)(e^{\beta\hbar\omega(q_1+q_2)}-1)} \right\}, \end{aligned} \quad (93)$$

$$\begin{aligned} \sigma^{(4)} &= \frac{9\hbar^3 a^3 k_{4eff}}{4\pi^3 k_{eff}^4} \int_0^{\pi/a} dq_1 \int_0^{\pi/a-q_1} dq_2 \int_{-\pi/a}^{\pi/a-(q_1+q_2)} dq_3 \frac{\omega(q_1)\omega(q_2)\omega(q_3)\omega(q_4)}{\omega(q_1)+\omega(q_2)+\omega(q_3)+\omega(q_4)} \\ &\times \left\{ 1 + 8 \frac{Z(q_1)Z(q_2)Z(q_3)-Z(q_4)}{(Z(q_1)-1)(Z(q_2)-1)(Z(q_3)-1)(Z(q_4)-1)} \frac{\omega(q_1)+\omega(q_2)+\omega(q_3)}{\omega(q_1)+\omega(q_2)+\omega(q_3)-\omega(q_4)} \right. \\ &\left. + 6 \frac{Z(q_1)Z(q_2)-Z(q_3)Z(q_4)}{(Z(q_1)-1)(Z(q_2)-1)(Z(q_3)-1)(Z(q_4)-1)} \frac{\omega(q_3)+\omega(q_4)}{\omega(q_1)+\omega(q_2)-\omega(q_3)-\omega(q_4)} \right\}, \end{aligned} \quad (94)$$

II.12.2. Numerical results and discussions

Hence, Figs. 23–25 illustrate the anharmonic effective potential and dispersion relation of Mo, Fe, W and four temperature-dependent cumulants of Mo calculated using the present ACDM and their Morse potential parameters [57]. They agree well with the experimental values [65], while those calculated using the SPP get significant discrepancies with experiment.

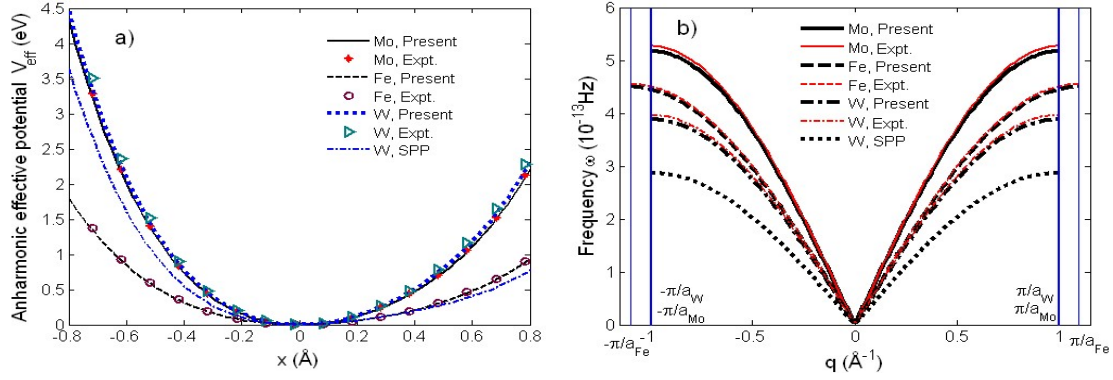


Fig. 23. (a) anharmonic effective potentials and (b) dispersion relations of Mo, Fe, W compared to the experimental values [65] and to those calculated using SPP.

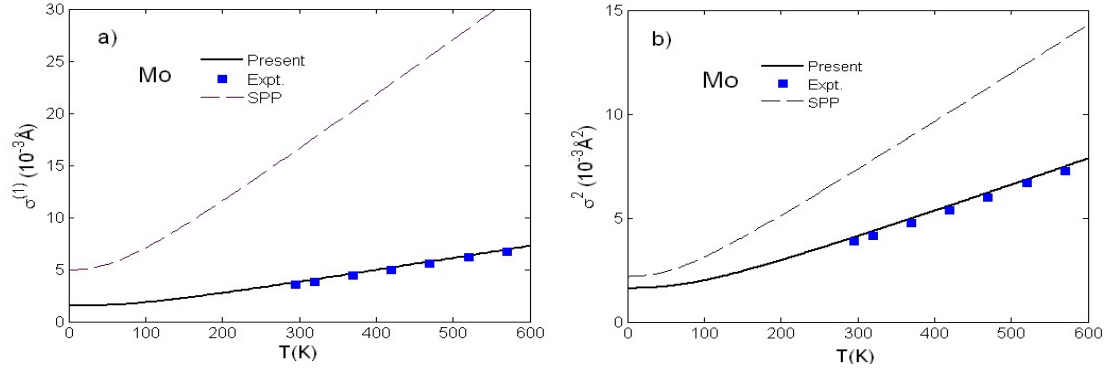


Fig. 24. Temperature dependence of (a) first cumulant $\sigma^{(1)}(T)$ and (b) second cumulant $\sigma^{(2)}(T)$ of Mo calculated using the present theory compared to the experimental values [65], and to those calculated using SPP.

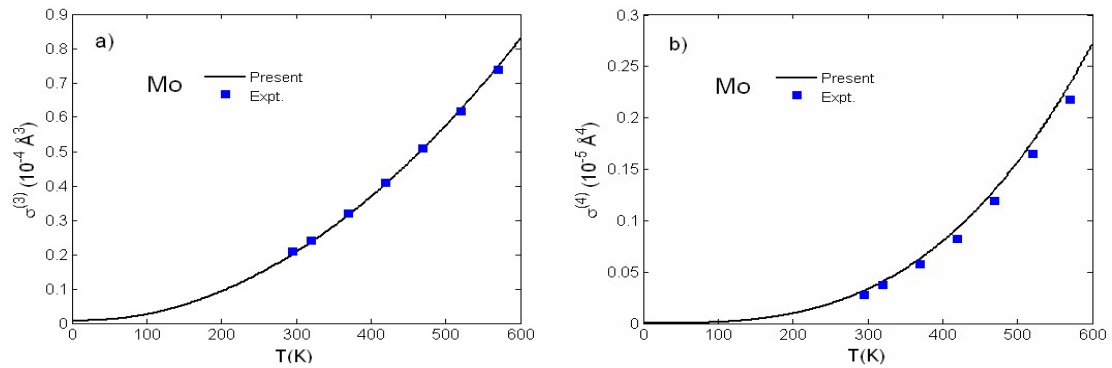


Fig. 25. Temperature dependence of (a) third cumulant $\sigma^{(3)}(T)$ and (b) fourth cumulant $\sigma^{(4)}(T)$ of Mo calculated using the present theory compared to the experimental values [65].

II.13. Pressure effects in DWF and in XAFS [35,47,48]

II.13.1. Derivation of method to study pressure effects in Debye-Waller factors and in XAFS

The main purpose of this work is including pressure effects in DWF presented in cumulant expansion and in XAFS. Using equation of state, AEP three first XAFS pressure dependent cumulants $\sigma^{(1)}$, σ^2 , $\sigma^{(3)}$ have resulted as

$$\begin{aligned}\sigma^2(P, T) &= \sigma_0^2(V(P)) \frac{1+z(V(P), T)}{1-z(V(P), T)}, \\ \sigma_0^2(V(P)) &= \frac{\hbar\omega_E(V(P))}{2k_{eff}(V(P))}, \\ z(V(P), T) &= \exp[-\theta_E(V(P))/T],\end{aligned}\tag{95}$$

$$\begin{aligned}\sigma^{(1)}(P, T) &= \sigma_0^{(1)}(V(P)) \frac{1+z(V(P), T)}{1-z(V(P), T)}, \\ \sigma_0^{(1)}(V(P)) &= f_1(\sigma_0^2(V(P))),\end{aligned}\tag{96}$$

$$\begin{aligned}\sigma^{(3)}(P, T) &= \sigma_0^{(3)}(V(P)) \frac{3(\sigma^2(V(P), T))^2 - 2(\sigma_0^2(V(P)))^2}{(\sigma_0^2(V(P)))^2}, \\ \sigma_0^{(3)}(V(P)) &= f_3(\sigma_0^2(V(P))),\end{aligned}\tag{97}$$

$$\begin{aligned}\omega_E(V(P)) &= \omega_E(V_0) \exp\left\{\gamma_G(V_0) \left[1 - \frac{V(P)}{V_0}\right]\right\}, \\ \theta_E(V(P)) &= \frac{\hbar\omega_E(V(P))}{k_B}, \\ \frac{V(P)}{V_0} &= \frac{a^3(P, T)}{a^3(0, 0)}.\end{aligned}\tag{98}$$

where $\sigma_0^{(1)}(V(P))$, $\sigma_0^2(V(P))$ and $\sigma_0^{(3)}(V(P))$ are pressure-dependent zero-point contributions to the first, second and third cumulants, respectively. They are described by the functions of the zero-point contribution to the second cumulant $\sigma_0^2(V(P))$ with explicit form depending on crystal structure and on using Morse or Lennard-Jones (L-J), potentials, as well as using ACEM or statistical moment method (SMM). Here, $\omega_E(P)$, $\theta_E(P)$, $a(P, T)$ are pressure-dependent correlated Einstein frequency and temperature, and the distance of the nearest neighboring atoms, respectively.

II.13.2. Numerical results and discussions

Hence, the above Figs. 26–27 illustrate the pressure effects calculated using the present theory evidenced in cumulants, in XAFS spectra and their Fourier transform magnitudes. They have the advantage of good agreement with experiment and with those of other methods.

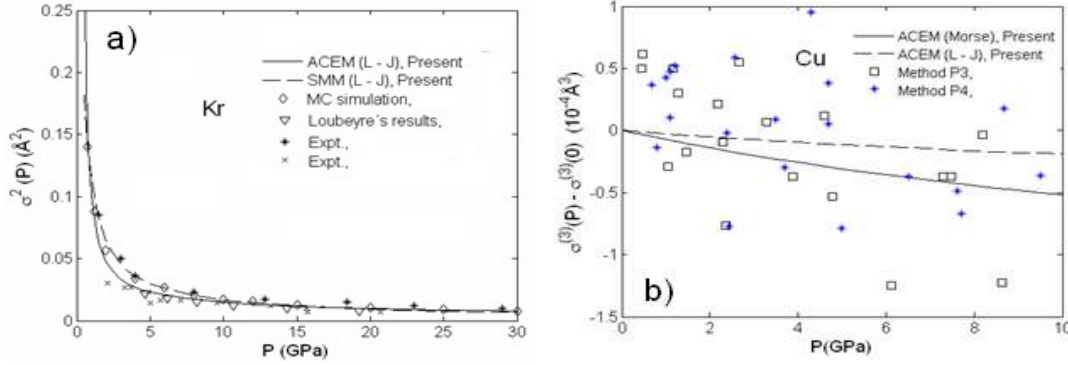


Fig. 26. Pressure dependence of (a) second cumulant $\sigma^2(P)$ or MSRD of Kr calculated by ACEM, SMM compared to the experimental values [68, 69], MC simulation [68], Loubeyre's method [69] results and (b) $\sigma^{(3)}(P) - \sigma^{(3)}(0)$ of Cu calculated by ACEM using Morse and (L-J) potentials compared to the results of P3 and P4 methods [68].

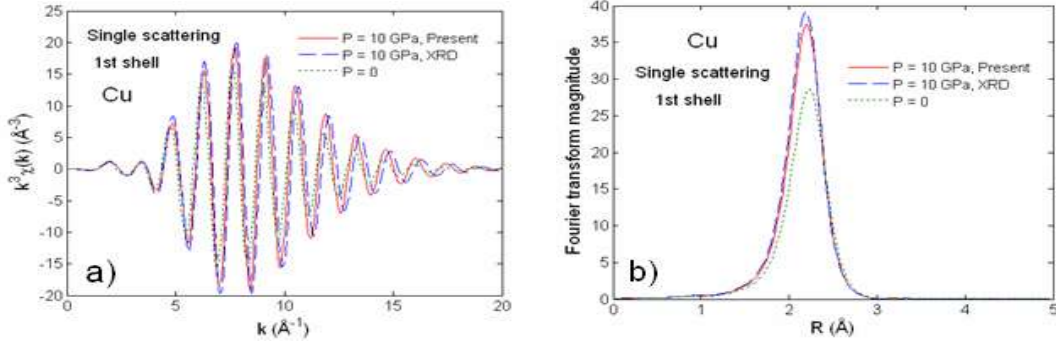


Fig. 27. (a) Pressure-dependent XAFS spectra of Cu and (b) their Fourier transform magnitudes.

II.14. Methods for studying thermodynamic properties of semiconductors [49–54]

II.14.1. Temperature-dependent Debye-Waller factors of semiconductors

Based on the GACEM (generalized ACEM) [49] the Debye-Waller factor presented in terms of three first temperature-dependent XAFS cumulants for semiconductors $\sigma^{(1)}(T)$, $\sigma^2(T)$, $\sigma^{(3)}(T)$ as

$$\sigma^{(1)}(T) = a = \sigma_0^{(1)} \frac{1 + z(T)}{1 - z(T)} = \frac{\sigma_0^{(1)}}{\sigma_0^2} \sigma^2(T), \quad \sigma_0^{(1)} = \frac{35}{83} \alpha \sigma_0^2, \quad (99)$$

$$\sigma^2(T) = \langle y^2 \rangle = \sigma_0^2 \frac{1 + z(T)}{1 - z(T)}, \quad \sigma_0^2 = \frac{\hbar \omega_E}{2k_{eff}}, \quad (100)$$

$$\sigma^{(3)}(T) = \langle y^3 \rangle = \sigma_0^{(3)} \left[3 \left(\sigma^2(T) / \sigma_0^2 \right)^2 - 2 \right], \quad \sigma_0^{(3)} = 15 \alpha \left(\sigma_0^2 \right)^2. \quad (101)$$

where $\sigma_0^{(1)}$, σ_0^2 , $\sigma_0^{(3)}$ are zero-point energy contributions to these cumulants, respectively.

Considering further in combination with SMM the analytical expressions of Debye-Waller factor (DWF) presented in terms of mean square displacement (MSD) of semiconductors having zinc-blende structure [47] have resulted.

II.14.2. Numerical results and discussions

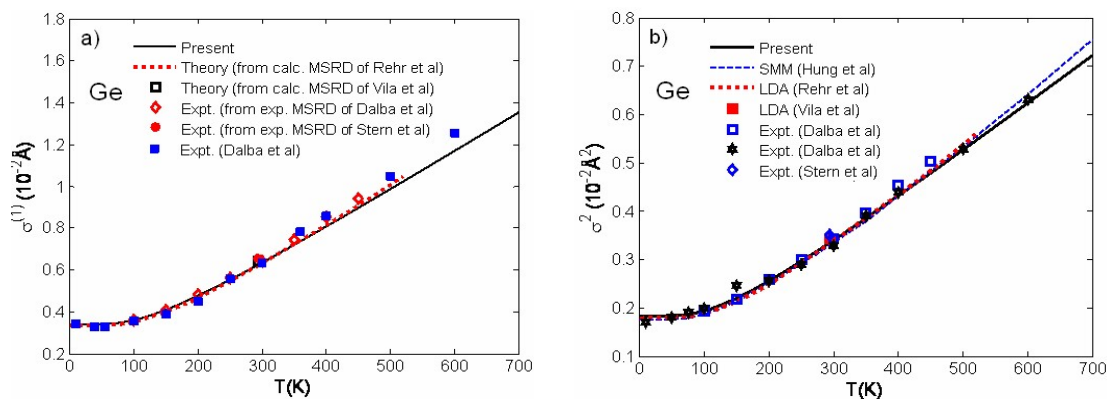


Fig. 28. Temperature dependence of (a) first cumulant $\sigma^{(1)}(T)$ calculated using the present theory for Ge compared to the experimental values [70], and to those calculated from the experimental (exp.) MSRD [71,72], as well as from the calculated (calc.) MSRD [73,74] and (b) second cumulant $\sigma^2(T)$ calculated using the present theory for Ge compared to the experimental values [70–72], and to those [73,74] calculated using LDA, and of N. V. Hung *et al.* [51].

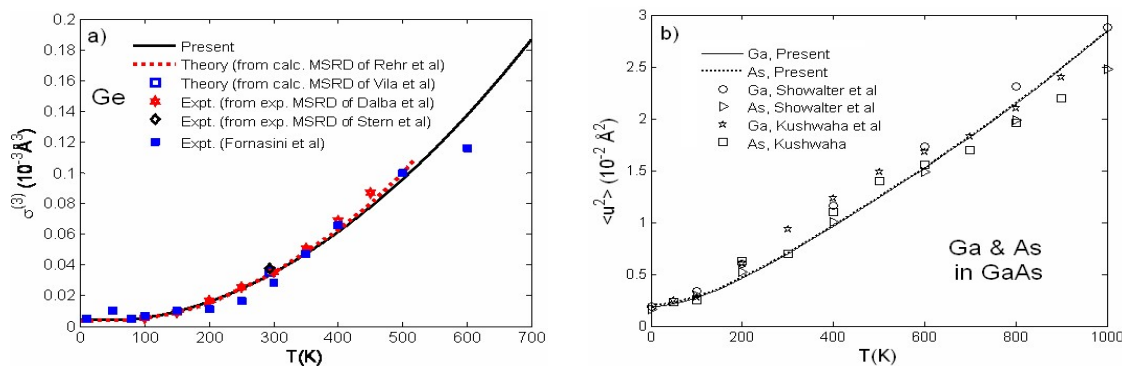


Fig. 29. Temperature dependence of (a) third cumulant $\sigma^{(3)}(T)$ calculated using the present theory for Ge compared to the XAFS experimental values [75], as well as to those calculated from the experimental (exp.) MSRD [70,72] and from the calculated (calc.) MSRD [73,74], and (b) MSD $\langle u^2(T) \rangle$ calculated by the present theory for Ga and As in GaAs compared to those of M. Showalter *et al.* [76] and of M. S. Kushwaha [77].

Note that the results calculated by the present theory presented in Figs. 28–29 agree well with experiment and with those calculated by other theories.

II.15. Deriving the method for studying correlation effects [46]

II.15.1. Correlation effects studied based on Debye-Waller factors

The displacement correlation function (DCF) $C_R(T)$ describing correlation effects is defined based on DWFs as

$$C_R(T) = 2 \langle (\mathbf{u}_0 \cdot \hat{\mathbf{R}}^0) (\mathbf{u}_i \cdot \hat{\mathbf{R}}^0) \rangle = 2u^2(T) - \sigma^2(T), \quad (102)$$

where $\mathbf{u}_0 = \mathbf{u}_i$ are the atomic displacements of the *zeroth* and the *ith* sites from their equilibrium, $\hat{\mathbf{R}}^0$ is the unit vector pointing from the *zeroth* site towards the *ith* site, $\sigma^2(T)$ and $u^2(T)$ are the MSRD and MSD, respectively.

Based on calculating $\sigma^2(T)$ and $u^2(T)$ for fcc crystals using the ACDM from Eq. (102) the function $C_R(T)$ has resulted and given by

$$C_R(T) = \frac{\hbar a}{2\pi D\alpha^2} \left\{ \frac{1}{4} \int_0^{\pi/a} \omega_1(q) \frac{1+z_1(q)}{1-z_1(q)} dq - \frac{1}{5} \int_0^{\pi/a} \omega(q) \frac{1+z(q)}{1-z(q)} dq \right\}, \quad |q| \leq \frac{\pi}{a}, \quad k_{eff}^S = 8D\alpha^2, \quad (103)$$

$$z_1(q) = \exp(\beta \hbar \omega_1(q)), \quad \omega_1(q) = 2\sqrt{\frac{k_{eff}^S}{M}} \left| \sin\left(\frac{qa}{2}\right) \right|,$$

$$z(q) = \exp(\beta \hbar \omega(q)), \quad \omega(q) = 2\sqrt{\frac{10D\alpha^2}{M}} \left| \sin\left(\frac{qa}{2}\right) \right|.$$

where M is the atomic mass, D and α are the Morse potential parameters.

II.15.2. Numerical results and discussions

Numerical calculations have been carried out using its Morse potential parameters [57]

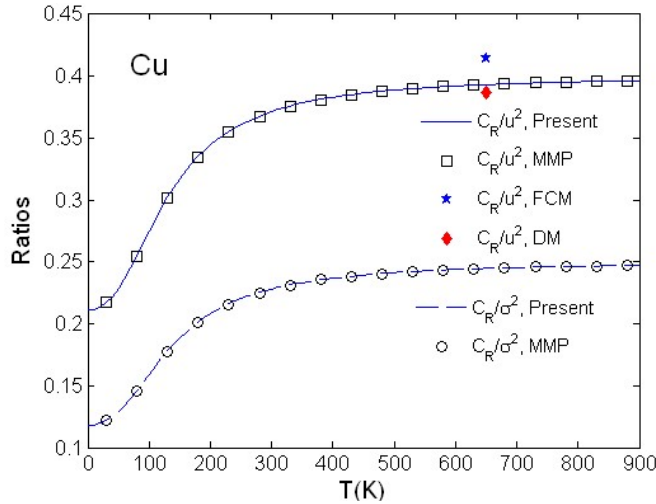


Fig. 30. Temperature dependence of the ratios C_R/u^2 and C_R/σ^2 of Cu calculated using the present theory compared to experiment obtained from the MMPs [65], as well as to the values calculated using the force constant model (FCM) [78] and Debye model (DM) [79] for the ratio C_R/u^2 .

Consequently, the results calculated using the present theory presented in Fig. 30 for C_R/u^2 agree well with experiment obtained from MMPs [65] and are found to be in reasonable agreement with those calculated using the force constant method (FCM) $C_R/u^2 = 0.415$ [78] and the Debye method (DM) $C_R/u^2 = 0.387$ [79]. Their constant values at high-temperatures indicates the similarity of temperature dependence of the considered functions $\sigma^2(T)$, $u^2(T)$ and $C_R(T)$ at these temperatures.

II.16. Derivation of theory for studying melting temperature [55–57]

II.16.1. Thermodynamic lattice theory on melting curve and eutectic point of binary alloys

The Lindemann's criterion on melting is based on the concept that the melting occurs when the ratio of the root mean square fluctuation (RMSF) in atomic positions on the equilibrium lattice positions and the nearest neighbor distance reaches a threshold value R . In the present theory based on DWF (MSD) at a given temperature T the quantity R defined by the ratio of the RMSF in atomic positions on the equilibrium lattice positions and the nearest neighbour distance d has resulted as

$$R = \frac{1}{d} \sqrt{\frac{9pm^2\hbar^2T}{M_1[s + (p-s)m]k_B\theta_D^2}}. \quad (104)$$

where each binary alloy lattice cell contains p atoms, where s is number of atoms of type 1 and $(p-s)$ is number of atoms of type 2, $m = M_1/M_2$ with M_1 , M_2 being atomic masses of elements 1 and 2.

Based on the Lindemann's criterion, the binary alloy will be melted when this ratio R reaches a threshold value R_m , then the Lindemann's melting temperature T_m for a binary alloy is derived as

$$T_m = \frac{[sM_2 + (p-s)M_1]}{9pm} \chi, \quad \chi = \frac{R_m^2 k_B \theta_D^2 d^2}{\hbar^2}, \quad R_m^2 = \frac{1}{Nd^2} \sum_n |U_{2n}|^2. \quad (105)$$

The average of χ can not be directly based on χ_1 and χ_2 because it has the form of Eq. (105) containing R_m^2 , i.e., the second order of R_m , while the other averages have been realized based on the first order of the displacement. That is why the average of $\chi^{1/2}$ will be performed

$$\chi = [s\sqrt{\chi_1} + (p-s)\sqrt{\chi_2}]^2 / p^2. \quad (106)$$

containing χ_1 for element type 1 and χ_2 for element type 2 having the following limiting values

$$\chi_2 = 9T_{m(2)}/M_2, \quad s = 0; \quad \chi_1 = 9T_{m(1)}/M_1, \quad s = p, \quad (107)$$

containing $T_{m(1)}$ and $T_{m(2)}$ as melting temperatures of the first or doping element and of the second or host element, respectively, composing the binary alloy.

II.16.2. Numerical results and discussions

Note that Table 1 and Fig. 31 illustrate good and reasonable agreement of the results calculated using the present theory with the experimental values [80]. The advantage of this theory is its possibility of providing melting temperatures of binary alloys with respect to any proportion of constituent elements.

Table 1. Calculated Lindemann's melting temperatures $T_m(K)$ of $\text{Cu}_{1-x}\text{Ni}_x$ and $\text{Cs}_{1-x}\text{Rb}_x$ with respect to different proportions x of Ni and Rb doped in Cu and Cs, respectively, compared to the experimental values [80].

x	0.10	0.30	0.50	0.70	0.90
$\text{Cu}_{1-x}\text{Ni}_x$, Present	1396	1468	1538	1611	1687
$\text{Cu}_{1-x}\text{Ni}_x$, Expt. [80]	1388	1461	1531	1605	1684
$\text{Cs}_{1-x}\text{Rb}_x$, Present	292.6	287.5	290.0	295.0	305.0
$\text{Cs}_{1-x}\text{Rb}_x$, Expt. [80]	291.4	286.0	287.4	293.5	304.0

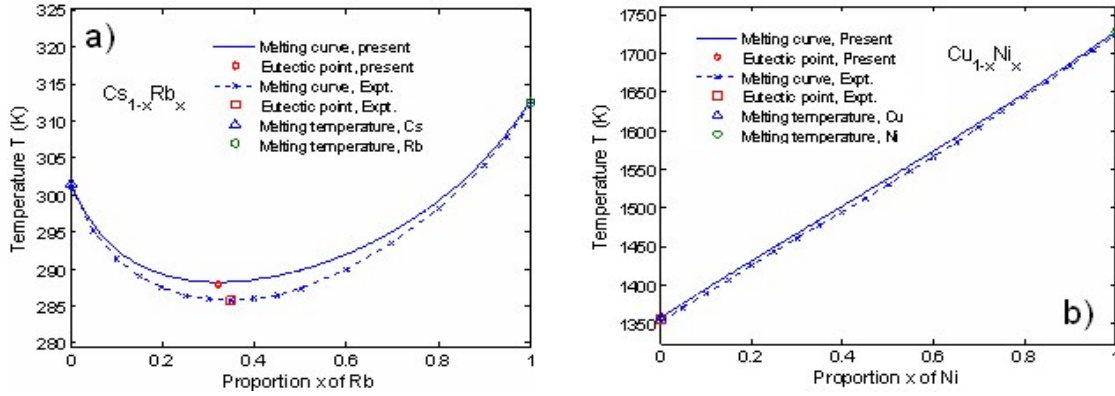


Fig. 31. Melting curves and eutectic points of binary alloys (a) $\text{Cs}_{1-x}\text{Rb}_x$ and (b) $\text{Cu}_{1-x}\text{Ni}_x$ calculated using the present theory compared to the experimental values [80].

III. CONCLUSIONS

The present article reviews several international publications [11-56] among 127 works of the author shown by brief descriptions of 16 contributions presented above. They include several new theories and models such as PDOS as a new physical quantity in ARPS, as well as the multiple-scattering theory, the anharmonic XAFS theory, the ACEM, the ACDM, the pressure-dependent ACEM, the classical ACEM, the ACEM for XAFS Mössbauer effect, the ACEMs for impurity, isotopic, pressure effects, the ACEM for semiconductors studies, the ACDM for correlation effects, and the thermodynamic lattice theory on melting curve and eutectic point of binary alloys.

The achieved developments contribute not only to providing different new theories and methods in the considered fields but also to overcoming limitations of some methods existed in the world, as well as to simplifying the complicated quantum and classical statistical tasks of many-body system into those of the one-dimensional model with taking many-body effects into account by a simple measure. They have been applied to different fields of materials studies not only in the theoretical researches but also in the experimental investigations providing good agreement of the calculated results with the measured values. Their publications involve the attentions of

scientists in the world leading to receiving 3.790 views and 716 citations (according to statistics of Mendeley in England [81] up to October 2020).

ACKNOWLEDGMENTS

The author thanks CIP for invitation to write this review article. The cooperation and useful comments in some researches of Professors J. J. Rehr, D. M. Pease (USA), P. Rennert, R. R. Frahm, B. Kirchner (Germany), P. Fornasini (Italy), and H. Kamitsubo (Japan) are highly appreciated.

REFERENCES

- [1] C. S. Fadley, S. A. L. Bergstroem, *Phys. Lett.* **35 A** (1971) 375.
- [2] B. Feuerbacher and R. F. Willis, *J. Phys. C* **9** (1976) 169.
- [3] M. J. Ambrosio and U. Thumm, *Phys. Rev. A* **96** (2017) 051403 (R).
- [4] Y. Ueda, Y. Suzuki, K. Watanabe, *Phys. Rev. B* **97** (2018) 075406.
- [5] E. D. Crozier, J. J. Rehr, and R. Ingalls, in *X-ray Absorption*, edited by D. C. Koningsberger and R. Prins (Wiley, New York, 1988).
- [6] E. A. Stern, P. Livins, Zhe Zhang, *Phys. Rev. B* **43** (1991) 8850.
- [7] A. I. Frenkel and J. J. Rehr, *Phys. Rev. B* **48** (1993) 585.
- [8] J. J. Rehr, J. Mustre de Leon, S. I. Sabinsky, R. C. Albert, *J. Am. Chem. Soc.* **113** (1991) 5135.
- [9] J. J. Rehr and R. C. Albers, *Rev. Mod. Phys.* **72** (2000) 621.
- [10] P. Fornasini, *J. Phys. Condens. Matter* **13** (2001) 7859.
- [11] P. Rennert and N. V. Hung, *Exp. Tech. Phys.* **26**(2) (1978) 151.
- [12] P. Rennert, N. V. Hung, *Exp. Tech. Phys.* **29**(1) (1981) 1- 6.
- [13] N. V. Hung and N. C. Toan, *Open Access J. Phys.* **3**(3) (2019) 25.
- [14] P. Rennert and N. V. Hung, *Proc. Int. Sym., Elec. Structure, Gaussig, Germany* (1986) 20.
- [15] P. Rennert and N. V. Hung, *Proc. Int. Sym., Elec. Structure, Gaussig, Germany* (1987) 16-20.
- [16] P. Rennert, N. V. Hung, *Phys. Stat. Sol. (b)* **148** (1988) 49-61.
- [17] N. V. Hung, *Exp. Tech. Phys.* **37** (1989) 203-212.
- [18] N. V. Hung and R. Frahm, *J. Phys. B* **208&209** (1995) 97-99.
- [19] N. V. Hung, *Proc. 4th. Int. Conf. on Syn. Rad. Sources; 2nd Forum on Syn. Rad. Kyongju, Korea* (1995) 420-424.
- [20] N. V. Hung, R. Frahm, H. Kamitsubo, *J. Phys. Soc. Jpn.* **65** (1996) 3571.
- [21] N. V. Hung, *J. de Physique IV* (1997) C2: 279-280.
- [22] N. V. Hung and J. J. Rehr, *Phys. Rev. B* **56**, No. 1 (1997) 43-46.
- [23] N. V. Hung, N. B. Duc, R. R. Frahm, *J. Phys. Soc. Jpn.* **72** (2003) 1254-1259.
- [24] N. V. Hung and P. Fornasini, *J. Phys. Soc. Jpn.*, Vol. **76**, No. 8 (2007) 084601.
- [25] N. V. Hung, T. S. Tien, L. H. Hung, R. R. Frahm, *Int. J. Mod. Phys. B* **22** (2008) 5155-5166.
- [26] M. Daniel, D. M. Pease, N. Van Hung, J. I. Budnick, *Phys. Rev. B* **69** (2004) 134414: 1-10.
- [27] D. Q. Vuong, N. V. Hung, *Mod. Phys. Lett. B*, 1950078 (12 pages) (2019).
- [28] N. V. Hung, C. S. Thang, N. B. Duc, D. Q. Vuong, T. S. Tien, *Phys. B* **521** (2017) 198.
- [29] N. V. Hung, C. S. Thang, N. B. Duc, D. Q. Vuong, T. S. Tien, *Eur. Phys. J. B*, **90** (2017) 256.
- [30] D. Q. Vuong and N. V. Hung, *Int. J. Adv. Appl. Phys. Research* **4**(2) (2017) 28.
- [31] T. S. Tien, N. B. Duc, H. D. Khoa, N. V. Hung, *J. Mater. Sci. Appl.* **4**(1) (2018) 10.
- [32] N. V. Hung, N. B. Duc, D. Q. Vuong, T. S. Tien, N. C. Toan, *Rad. Phys. Chem.* **80** (2021) 109263.
- [33] N. V. Hung, T. S. Tien, N. B. Duc, D. Q. Vuong, *Mod. Phys. Lett. B* **28** (2014) 1450174.
- [34] T. S. Tien, N. V. Hung, N. T. Tuan, N. V. Nam, N. Q. An, N. T. M. Thuy, V. T. K. Lien, N. V. Nghia, *J. Phys. Chem. Sol.* **134** (2019) 307.
- [35] N. V. Hung, *J. Phys. Soc. Jpn.* **83** (2014) 024802.1-6.
- [36] N. V. Hung, N. B. Trung, B. Kirchner, *Phys. B* **405** (2010) 2519-2525.
- [37] N. V. Hung, N. B. Trung, D. D. Son, T. S. Tien, N. B. Duc, *J. Phys. Sci. Appl.* **4**(1) (2014) 43.
- [38] N. V. Hung and D. Q. Vuong, *Int. J. Mod. Phys. Appl.* **1**(2) (2015) 32.
- [39] N. B. Trung, N. V. Hung and H. D. Khoa, *Int. J. Adv. Mater. Research* **2**(4) (2016) 52.

- [40] N. V. Hung, N. B. Trung and N. B. Duc, *J. Mater. Sci. Appl.* **1**(2) (2015) 51.
- [41] N. V. Hung, T. T. Hue, H. D. Khoa and D. Q. Vuong, *Phys. B* **503** (2016) 174.
- [42] N. V. Hung, T. T. Hue, N. B. Duc, D. Q. Vuong, *J. Chem. & Mater. Research*, **5** (2016) 99-104.
- [43] D. Q. Vuong and N. V. Hung, *Am. J. Electromagn. Appl.* **4**(2) (2016) 14.
- [44] N. B. Duc, V. Q. Tho, N. V. Hung, D. Q. Khoa and H. K. Hieu, *VAC*. **145** (2017) 272.
- [45] N. B. Duc, N. V. Hung, H. D. Khoa, D. Q. Vuong, T. S. Tien, *Adv. Mater. Sci. Engin.* **2018** (2018) 3263170.
- [46] N. V. Hung and D. Q. Vuong, *Mod. Phys. Lett. B* **33** (2019) 1950237.
- [47] N. V. Hung, V. V. Hung, H. K. Hieu and R. R. Frahm, *Phys. B* **406** (2011) 456.
- [48] H. K. Hieu, N. B. Duc, N. V. Hung, P. T. M. Hanh, and T. T. Hai, *J. Synch. Rad.* **27** (2020) 1.
- [49] N. V. Hung, N. B. Duc, D. Q. Vuong, N. C. Toan and T. S. Tien, *VAC*. **169** (2019) 108872.
- [50] N. C. Toan and N. V. Hung, *Glob. J. Engineer. Sci.* **3** (5) (2019) 1.
- [51] N. V. Hung, C. S. Thang, N. C. Toan, H. K. Hieu, *VAC*. **101** (2014) 63-66.
- [52] N. V. Hung, N. C. Toan, N. B. Duc, D. Q. Vuong, *Cent. Eur. J. Phys.* **13** (2015) 242.
- [53] N. V. Hung and H. D. Khoa, *Int. J. Mod. Phys. Appl.* **3** (6) (2016) 70-74.
- [54] H. D. Khoa, T. S. Tien, N. V. Hung, *J. Chem. & Mater. Research Vol.* **5** (6) (2016) 110-114.
- [55] N. V. Hung, Dung T. Tran, N. C. Toan, B. Kirchner, *Cent. Eur. J. Phys.* **9**(1) (2011) 222-229.
- [56] N. C. Toan, N. V. Hung, N. B. Duc, D. Q. Vuong, *Int. J. Adv. Mater. Research* **2**(5) (2016) 80.
- [57] L. A. Girifalco and W. G. Weizer, *Phys. Rev.* **114** (1959) 687.
- [58] R. P. Feynman, *Statistical Mechanics*, Benjamin Reading, 1972.
- [59] S. a Beccara, G. Dalba, P. Fornasini, R. Grisenti, F. Pederiva, A. Sanson, D. Diop and F. Rocca, *Phys. Rev. B* **68** (2003) 140301(R).
- [60] R. B. Greeger and F. W. Lytle, *Phys. Rev. B* **20** (1979) 4908.
- [61] T. Yokoyama, T. Susukawa, and T. Ohta, *Jpn. J. Appl. Phys.* **28** (1989) 1905.
- [62] Y. S. Toukian, R. K. Kirby, R. E. Taylor, and P. D. Desai, *Thermophysical Properties of Matter* (IFI/Plenum, New York, 1975).
- [63] N. V. Hung, *Comm. Phys.* **14** (2004) 7.
- [64] Professor Douglas M. Pease, Dept. Phys., University of Connecticut, Condensed Matter Physics Seminar, TU <http://phys.uconn.edu/seminars/2004.../200402cmp.htm> UT (2004).
- [65] I. V. Pirog and T. I. Nedoseikina, *Phys. B* **334** (2003) 123.
- [66] J. Purants, N. D. Afify, G. Dalba, R. Grisenti, S. De Panfilis, A. Kuzmin, V. I. Ozohomin, F. Rocca, A. Samson, S. I. Tiutiunnikov, and P. Fornasini, *Phys. Rev. Lett.* **100** (2008) 055901.
- [67] *American Institute of Physics Handbook*, 3rd ed. (AIP, New York, 1972) pp. 4-100.
- [68] J. Freund, R. Ingalls, and E. D. Crozier, *Phys. Rev. B* **39** (1989) 12537.
- [69] A. Di Cicco, A. Filippini, J. P. Itie, A. Polian, *Phys. Rev. B* **54** (1996) 9086.
- [70] G. Dalba, P. Fornasini, R. Grisenti and J. Purans, *J. Synch. Rad.* **6** (1999) 532.
- [71] G. Dalba, P. Fornasini, D. Diop, M. Grazioli, F. Rocca, *J. Non-Crys. Sol.* **164** (1993) 159.
- [72] A. E. Stern, B. A. Bunker, S. M. Heald, *Phys. Rev. B* **21** (1980) 5521.
- [73] F. D. Vila, J. J. Rehr, H. H. Rossner, H. J. Krappe, *Phys. Rev. B* **76** (2007) 014301.
- [74] J. J. Rehr, J. J. Kas, M. P. Prange, A. P. Soreni, Y. Takimoto and F. Vila, *C. R. Phys.* **10** (2009) 548.
- [75] P. Fornasini, S. A. Beccara, G. Dalba, R. Grisenti, A. Sanson and M. Vaccari, *Phys. Rev. B* **70** (2004) 174301.
- [76] M. Schowalter, A. Rosenauer, J. T. Titantah, D. Lamoen, *Acta Cryst. A* **65** (2009) 5.
- [77] M. S. Kushwaha, *Phys. Rev. B* **24** (1981) 2115.
- [78] R. M. Nicolow, G. Gilat, H. G. Smith, R. J. Raubenheimer, M. K. Wikinson, *Phys. Rev.* **164** (1967) 922.
- [79] G. Beni and P. M. Platzman, *Phys. Rev. B* **14** (1976) 1514.
- [80] T. B. Massalski, *Binary Alloy Phase Diagrams*, 2nd ed. (ASM Inter. Materials Parks, OH, 1990)
- [81] Mendeley Limited. Registered office The Boulevard, Langford Lane, Kidlington, Oxford, OX5 1GB, United Kingdom. Registered in England and Wales. Registration number 06419015.